AD-A042 656 PROTOTYPE DEVELOPMENT ASSOCIATES INC SANTA ANA CALIF F/G 16/3
EROSION MECHANICS AND MICROMECHANICS PROGRAM.(U)
JUL 77 J D BUCH N00014-75-C-1036
UNCLASSIFIED PDA-TR-1039-00-01 NL

1 OF 1
ADA042-656

END
DATE FILMED
8-77
DDC

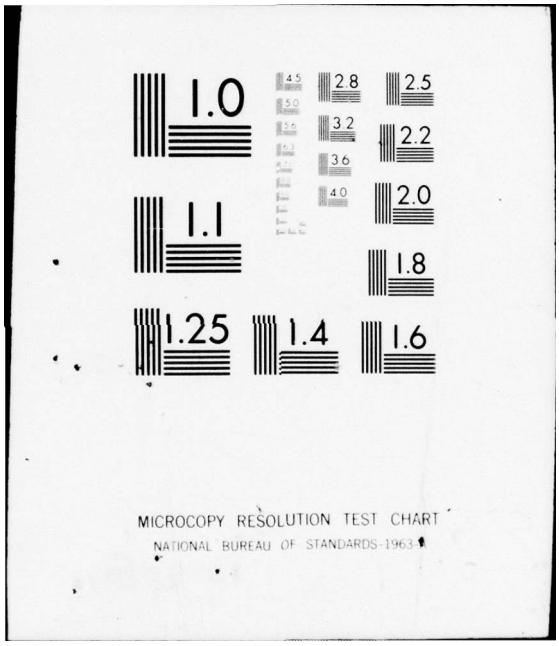
1.0
1.1
1.25
1.4
1.6
1.8
2.0
2.2
2.5
2.8
3.2
3.6
4.0
4.5
5.0
5.6
MICROCOPY RESOLUTION TEST CHART
NATIONAL BUREAU OF STANDARDS-1963-A

9

12

PDA, inc.
PROTOTYPE DEVELOPMENT ASSOCIATES

(12)

PDA TR 1039-00-01

EROSION MECHANICS AND MICROMECHANICS PROGRAM FINAL REPORT

Prepared for

OFFICE OF NAVAL RESEARCH
800 N. Quincy Street
Arlington, Virginia 22217

Under Contract No. N00014-75-C-1036

Prepared by

PROTOTYPE DEVELOPMENT ASSOCIATES, INC.
1740 Garry Avenue
Santa Ana, California 92705

UNCLASSIFIED

SECURITY CLASSIFICATION OF THIS PAGE (When Data Entered)

REPORT DOCUMENTATION PAGE

READ INSTRUCTIONS BEFORE COMPLETING FORM

1. REPORT NUMBER

2. GOVT ACCESSION NO.

3. RECIPIENT'S CATALOG NUMBER

4. TITLE (and Subtitle)

EROSION MECHANICS AND MICROMECHANICS PROGRAM,

5. TYPE OF REPORT & PERIOD COVERED

Final Report - 18 May 1975-18 Aug 76, 18 August 1976

6. PERFORMING ORG. REPORT NUMBER

PDA-TR-1039-00-01

7. AUTHOR(s)

J. D. Buch

8. CONTRACT OR GRANT NUMBER(s)

N00014-75-C-1036 new

9. PERFORMING ORGANIZATION NAME AND ADDRESS

Prototype Development Associates, Inc.
1740 Garry Avenue
Santa Ana, California 92705

10. PROGRAM ELEMENT, PROJECT, TASK AREA & WORK UNIT NUMBERS

61153N, RR022-02-01, NR032-555 RR0220201

11. CONTROLLING OFFICE NAME AND ADDRESS

Office of Naval Research
800 N. Quincy Street
Arlington, Virginia 22217

12. REPORT DATE

July 1977

13. NUMBER OF PAGES

58 63p.

14. MONITORING AGENCY NAME & ADDRESS (if different from Controlling Office)

15. SECURITY CLASS. (of this report)

Unclassified

15a. DECLASSIFICATION DOWNGRADING SCHEDULE

16. DISTRIBUTION STATEMENT (of this Report)

Unlimited

DISTRIBUTION STATEMENT A
Approved for public release;
Distribution Unlimited

17. DISTRIBUTION STATEMENT (of the abstract entered in Block 20, if different from Report)

18. SUPPLEMENTARY NOTES

19. KEY WORDS (Continue on reverse side if necessary and identify by block number)

Dynamic Analyses	Micromechanics	Wave Propagation
Erosion	Particle Impact	Weather Survivability
Fracture Mechanics	Rain Erosion	
IR Windows	Structural Mechanics	

20. ABSTRACT (Continue on reverse side if necessary and identify by block number)

The objectives of this study were to provide the basic understanding of the particle impact phenomena which produce damage in IR windows in order to establish material development guidelines, to predict performance under anticipated operational conditions, to define failure conditions, to establish the technical base on which extrapolation into high velocity impact regimes can be carried out, and to extend the understanding of material behavior into the transitional regime between low velocity rain erosion processes important to IR and optical windows and the hypervelocity reentry conditions which are critical to reentry vehicle designs.

DD FORM 1 JAN 73 1473 EDITION OF 1 NOV 65 IS OBSOLETE

UNCLASSIFIED

SECURITY CLASSIFICATION OF THIS PAGE (When Data Entered)

390714

A series of three dynamic particle impact analyses were carried out for PDA at California Research and Technology, Inc. using their WAVE-L computer program. A study of material fracture and micromechanics consideration led to an understanding of the material behavior associated with particle impact.

Specific accomplishments of the study include a theoretical explanation of the Rochester and Brunton experimental observations of off-axis pressure peaking for water particle impact, the discovery of major tensile components of the three-dimensional stress field not predicted accurately by static Hertzian analyses, and the formulation of a combined micromechanics and macromechanics analysis technique associated with the flaw distribution characteristics of the material being analyzed.

TABLE OF CONTENTS

1.0 INTRODUCTION AND SUMMARY

The behavior of materials under particle impact is of critical importance in the performance of IR windows, nosetips and heatshields and turbine blade applications. The applications have been roughly classed as high and low velocity encounters with a minimum of interaction between the techniques used to investigate performance in these different velocity regimes. While such a separation has thus far been practical, the extension of missile performance to higher velocities (e.g., Mach 2.5-3.0) and anticipated performance in the Mach 5.0 and 6.0 range, make it necessary to broaden the base of understanding of material behavior in order to predict material behavior under conditions not previously investigated. The objectives of the program are:

1. Provide the basic understanding of the particle impact phenomena which produce damage in IR windows in order to establish material development guidelines, predict performance under anticipated operational conditions and define failure conditions.
2. To establish the technical base on which extrapolation into high velocity regimes can be carried out.
3. To extend the understanding of material behavior into the transitional regime between low velocity rain erosion processes important to IR and optical windows and the hypervelocity reentry conditions which are critical to reentry vehicle design.

The erosion/degradation problem can be and has been addressed from the viewpoints of empirical materials development, microstructural studies, dynamic code analysis of the impact event, and static (Hertzian indentation) analysis and experimental simulation. Currently lacking is a framework for logically connecting these separate approaches, particularly making the low to high velocity transition. Establishment of such a framework, its application, and correlation with experiment constitutes the basis of the present effort.

Unique key elements of the program are 1) providing the computational framework for translating dynamic code analysis of the impact event into a form

suitable for microstructural and micromechanical formulation of the damage event, 2) the accompanying microstructural and micromechanical formulation of single and multiple impact phenomena, and 3) correlation of the damage predictions with existing data.

The outputs from the program are 1) improved integration of the currently utilized approaches, 2) delineation of the velocity conditions under which static linear formulations become inadequate as well as when nonlinear approaches are necessary, 3) coupling of code solutions to micromechanics and damage formulations, 4) sensitivity of damage to macroscopic and microstructural material parameters, and 5) a logical formal transition between single and multiple impact phenomena.

The benefits from the program are 1) a baseline technique with which to examine many velocity ranges and applications, 2) a baseline technique capable of adaptation to impact code improvements or other impact codes, 3) an integrated approach to formulating material development guidelines, and 4) a formulation sufficiently general to allow low to high velocity encounter transitions.

Specific tasks pursued under this contract are summarized below:

Task I. Impact of a Water Drop on a Rigid Surface

Impact surface pressure distributions were determined by the WAVE-L computer code under subcontract to California Research and Technology, Inc. (CaRT). The scope of the effort was centered upon resolving the early time off-axis peaking reported by Rochester and Brunton and as evidenced in previous water drop simulations by CaRT.

Task II. Numerical Calculations of an 1100 FPS and 4000 FPS Impact of 290 Micron Glass Spheres on a ZnSe Plate

The impact event was subjected to static and Hertzian analysis. The static analysis was taken from well-known forms in the technical literature and simulated the theoretical impact pressure distributions.

Dynamic analyses were accomplished by the linear elastic options available in the WAVE-L code which formed the baseline analytical technique. Two impact velocities were considered. The surface pressure distributions were taken as those indicated directly by impact experiments.

The results of the static and dynamic computations were compared to assess the range of validity of static and dynamic stress models and the significance of nonlinear mechanics to the velocity range of interest.

Task III. Crack Nucleation and Growth from Low Velocity Particle Impact on Brittle Materials

Stresses were examined at various times by micromechanical methods. These included statistical distributions of fracture initiation sites, multiple crack initiation, slow and fast crack growth concepts, and crack coalescence. Micromechanical variables were varied to define critical material concepts.

The outputs of the analyses were correlated with available data to provide direction for improved damage modeling, as well as preliminary guidelines for material improvement. Definition of critical theoretical and experimental concepts were accomplished.

The following three sections discuss the results of each of the three major tasks of the Erosion Mechanics and Micromechanics Program. Conclusions are summarized in Section 5.0.

2.0 IMPACT OF A WATER DROP ON A RIGID SURFACE

2.1 Introduction

Previous experimental, theoretical, and numerical studies (Refs. 1, 2, 3) indicate that when a water drop impacts a relatively rigid surface, an early time pressure peak occurs on the surface somewhat off the impact axis. This pressure peak may exceed the "waterhammer" pressure ($\rho_o C_o V_o$) by factors of two to three. This phenomenon is of practical importance since the pressure pulse could activate crack propagation in brittle targets by forcing high pressure water into surface openings.

In this study, a finely-resolved two-dimensional numerical solution was performed to specifically investigate this pressure pulse using the Lagrangian finite difference WAVE-L code (Ref. 4). The water is initially divided into a number of axisymmetric volume elements, or cells, each of which has a pressure, internal energy, density, and particle velocities associated with it. The equations for updating the cell variables during a time cycle are obtained from finite difference analogues of the differential equations for conservation of mass, momentum, and energy, and the compressible material properties of the water. The material interface between the water drop and the rigid target was treated as frictionless. A definitive study of the pressures associated with liquid drop impingement is clearly desirable and is the goal of the present study.

2.2 Results of the Numerical Calculation

Figure 1 shows the (initial) computational grid used for describing the 1 mm diameter water drop impact event. The impact velocity (V_o) is 1100 fps. Figure 2 shows the velocity field (using the scale bar shown on the figure) for material in the vicinity of the impact site at .02 μ sec after the impact. The contact radius (r_c) is about .008 cm at this time. Notice the tendency of the velocity vectors in a roughly triangular region to focus toward the contact radius. Note also that near the radius of contact the particle velocity is not arrested, as in the calculation of the one-dimensional waterhammer pressure, but is deflected. Figure 3 shows

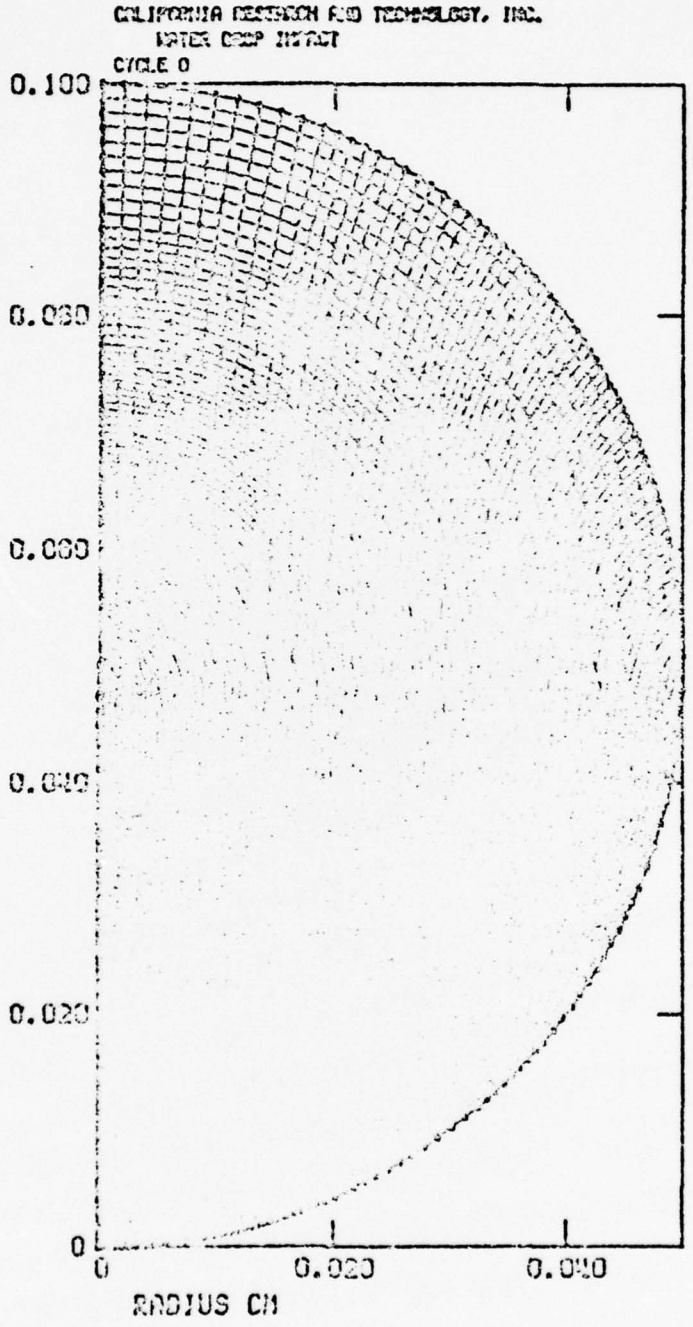

Figure 1. Initial Computational Grid for 1 mm Water Drop Impacting a Rigid Surface at 1100 fps.

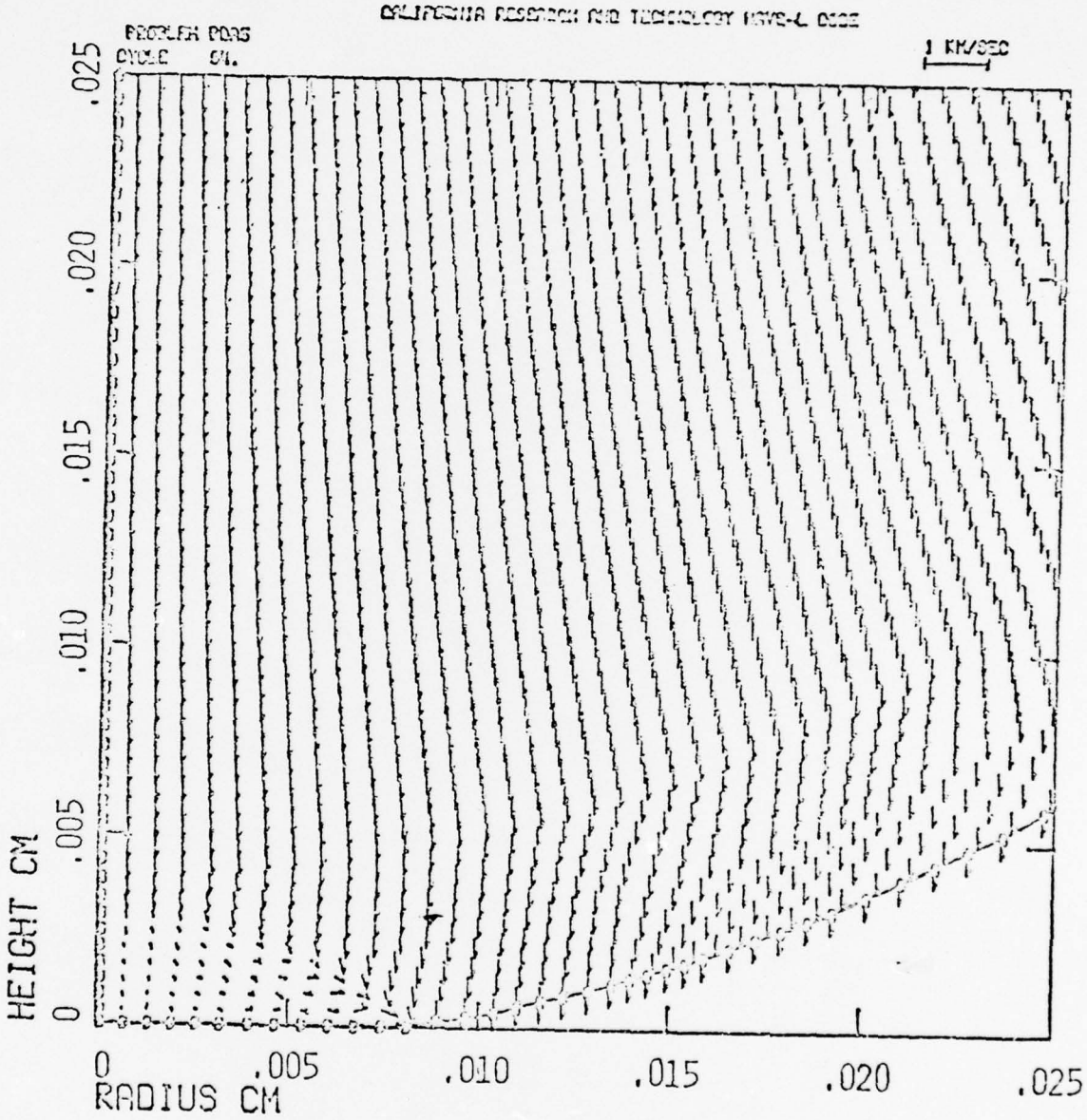

Figure 2. Velocity Field at 0.02 μsec.

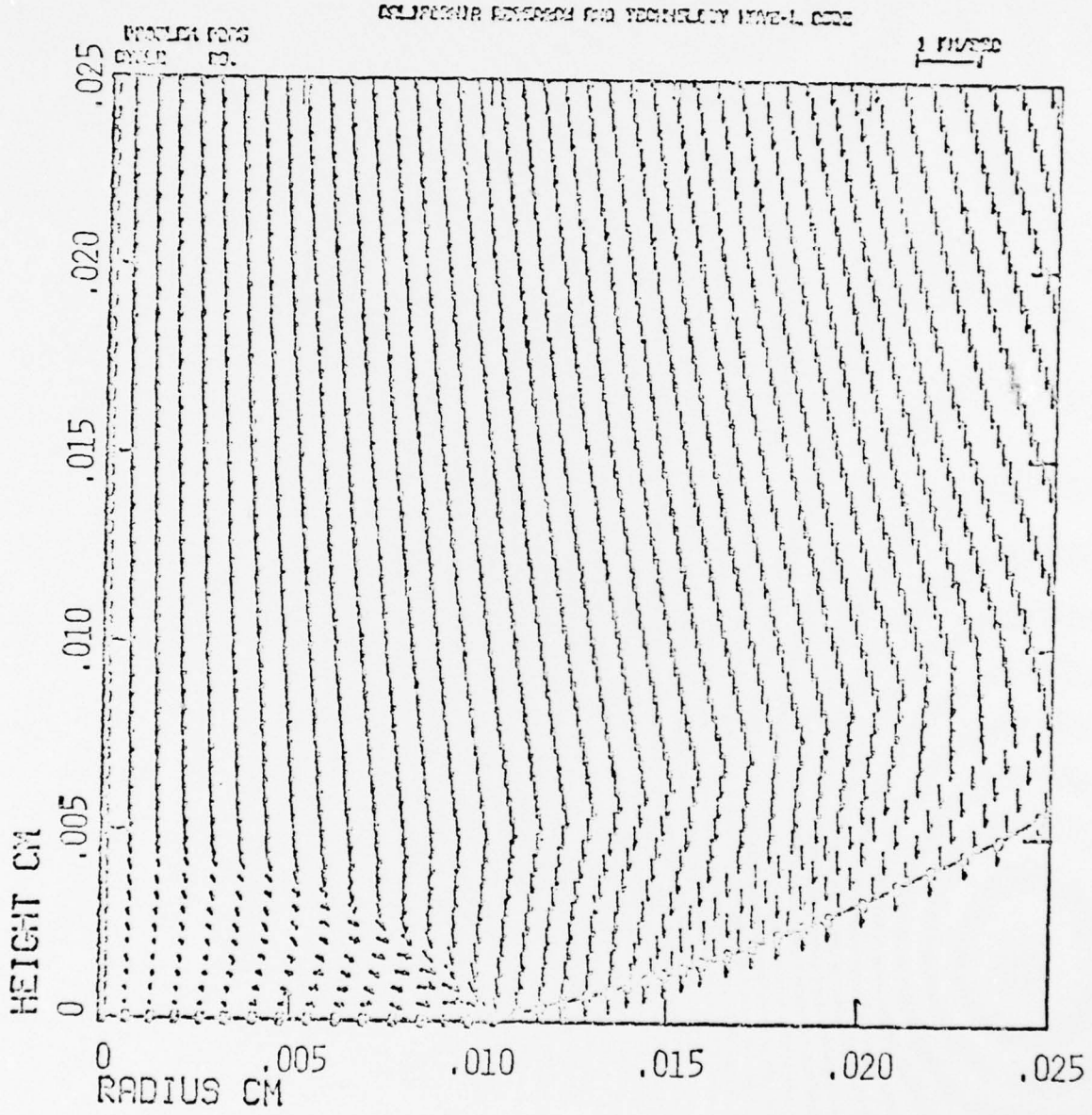

Figure 3. Velocity Field at 0.03 μsec.

the velocity field at .03 μsec. The focusing of the velocity vectors toward the contact radius is more evident in this figure. At this time the contact radius (r_c) is moving outward at a velocity ($\dot{r}_c$) only slightly greater than the sound speed (C_o) in undisturbed water. As will be shown below, the pressure peak occurs near the contact radius and continues to increase in magnitude as long as $\dot{r}_c$ is greater than C_o. Figure 4 shows the velocity field at .05 μsec. The convergence toward the contact radius is still qualitatively apparent; however, the influence of the free surfaces near the contact radius have reduced the peak pressure. By .09 μsec, as indicated in Figure 5, the velocity field is no longer strongly convergent toward the contact radius. Figure 5 also shows the very early stages of the formation of a cylindrically symmetric jet. (The calculation was terminated at .09 μsec, and thus the subsequent interaction between the jet and the water drop was not computed.)

The pressure-radius profiles on the target surface are shown for three times in Figure 6. Note that the waterhammer pressure ($\rho_o V_o C_o$) equals 5 kbars in this case. The pressure near the axis of cylindrical symmetry remains roughly at the waterhammer pressure; however, as time proceeds to .033 μsec a pressure peak is observed near the contact radius. The pressure peak reaches about 2.7 times the waterhammer pressure at .033 μsec.

Figure 7 shows pressure versus time profiles at several radii on the impact surface. The peak pressure occurs at about a radius of .01 cm or .2 of the droplet radius. Beyond this radius, the peak stress begins to fall off. Figure 8 shows the peak pressure versus radius at times prior to .09 μsec.

Figure 9 summarizes the relationships between contact radius speed ($\dot{r}_c$), water sound speed (C_o), and the timing of the maximum pressure predicted in the numerical calculation. The rate of increase of the contact radius ($\dot{r}_c$) as a function of time (t) can be obtained by assuming the spherical droplet (radius R) remains undeformed where it is not in contact with the rigid boundary. The geometry is indicated in Figure 9.

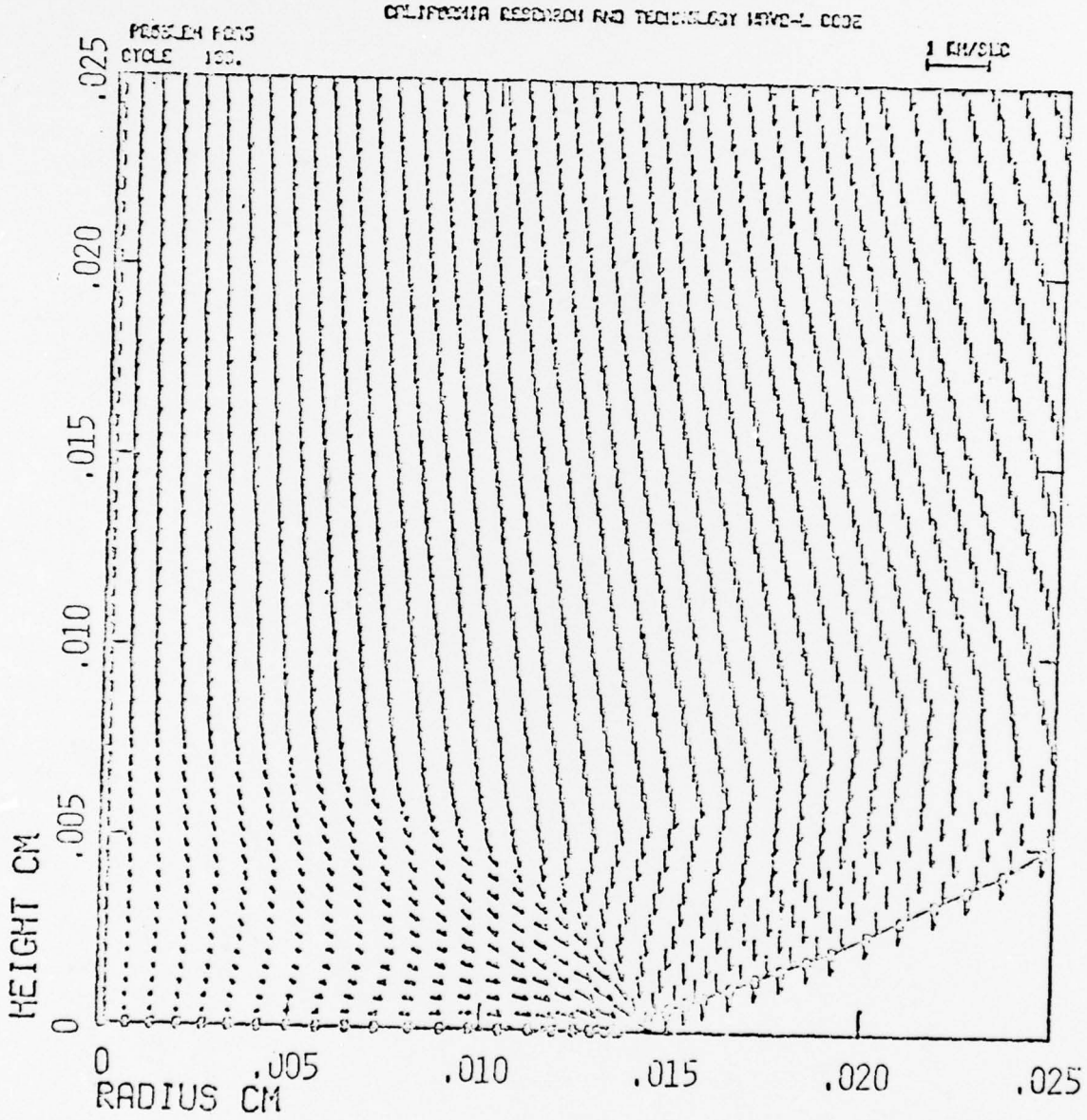

Figure 4. Velocity Field at 0.05 μsec.

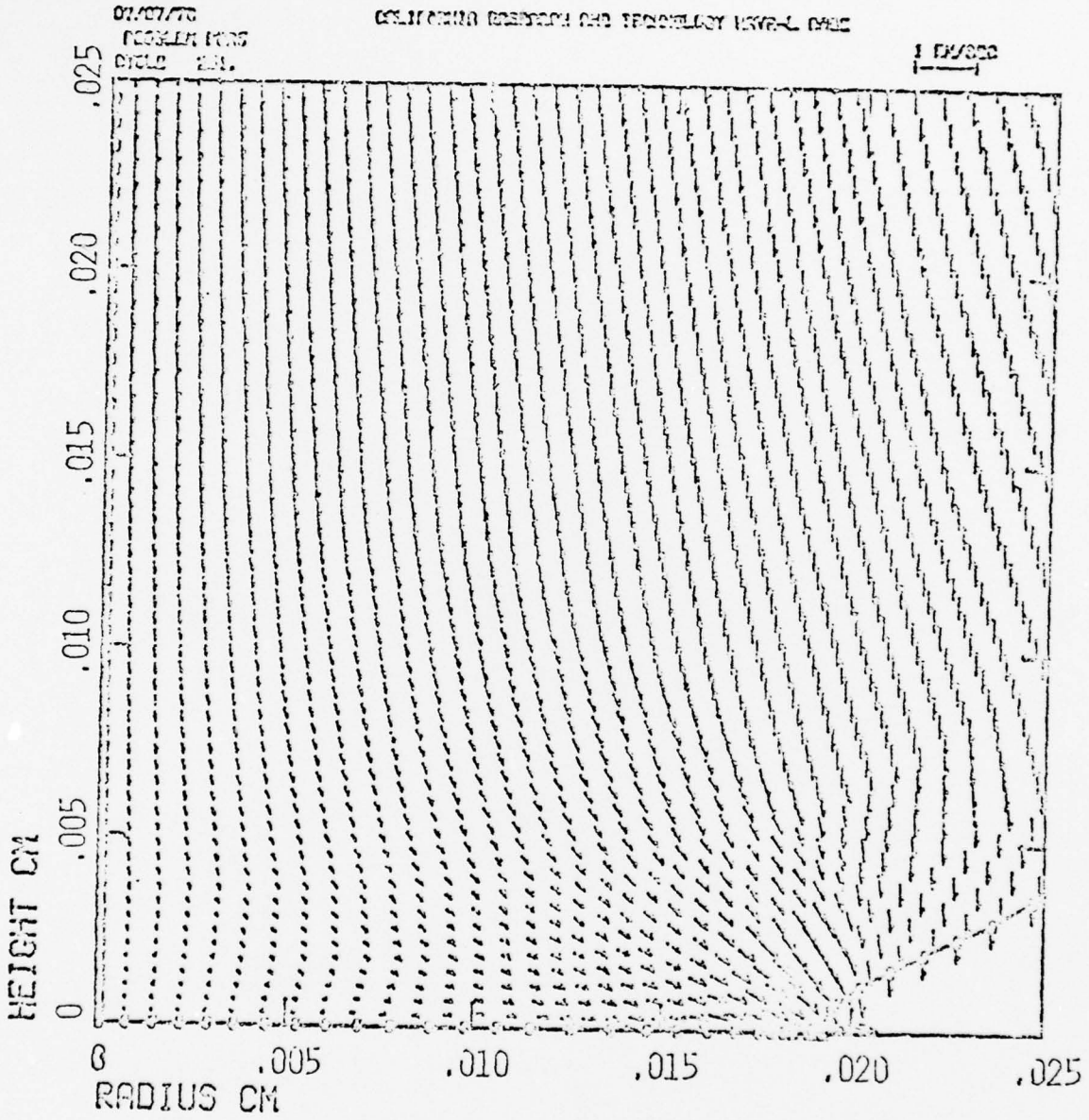

Figure 5. Velocity Field at 0.09 μsec.

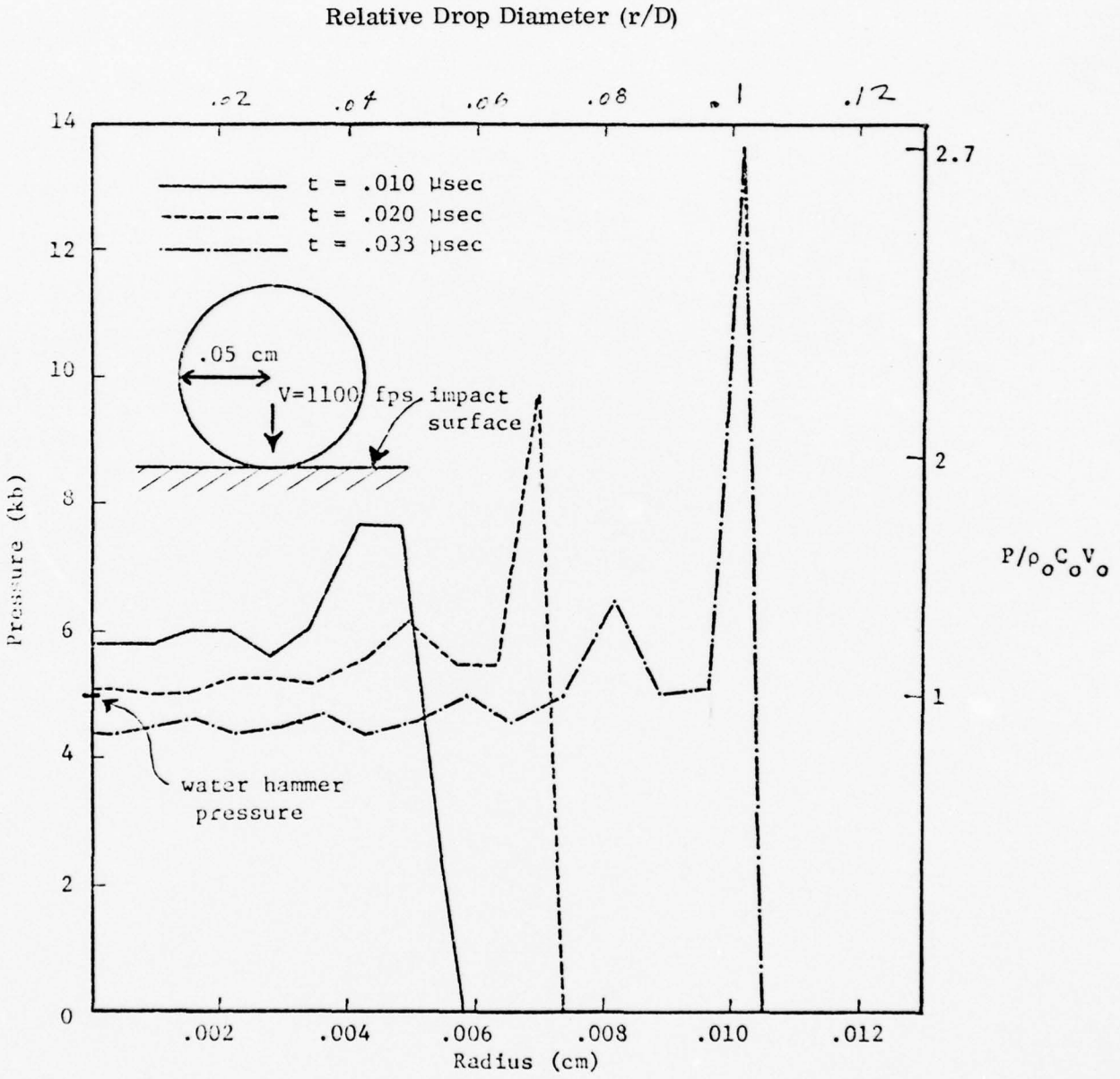

Figure 6. Pressure Vs. Radius on the Impact Surface at Several Times.

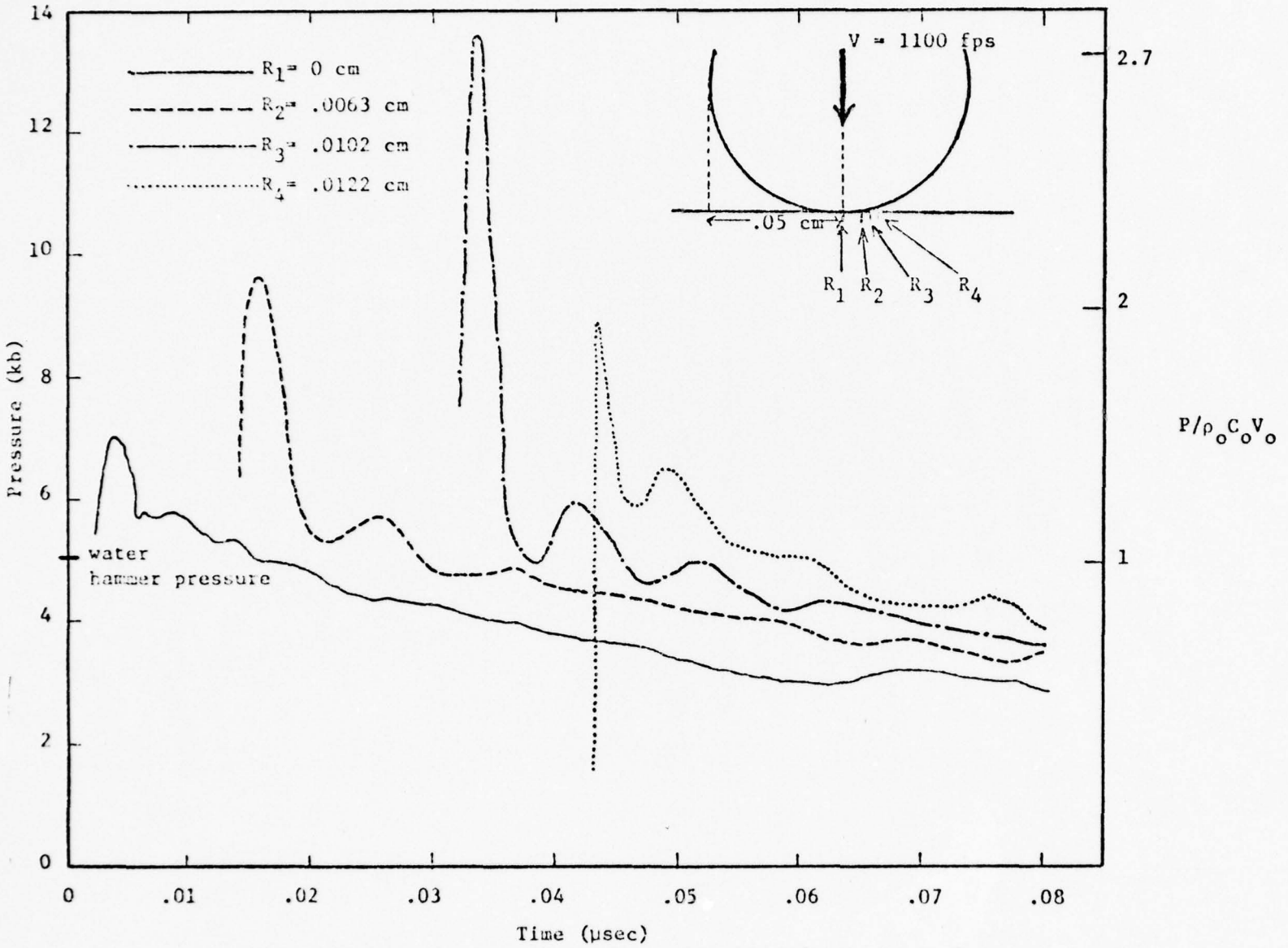

Figure 7. Pressure Vs. Time at Several Radii on the Impact Surface

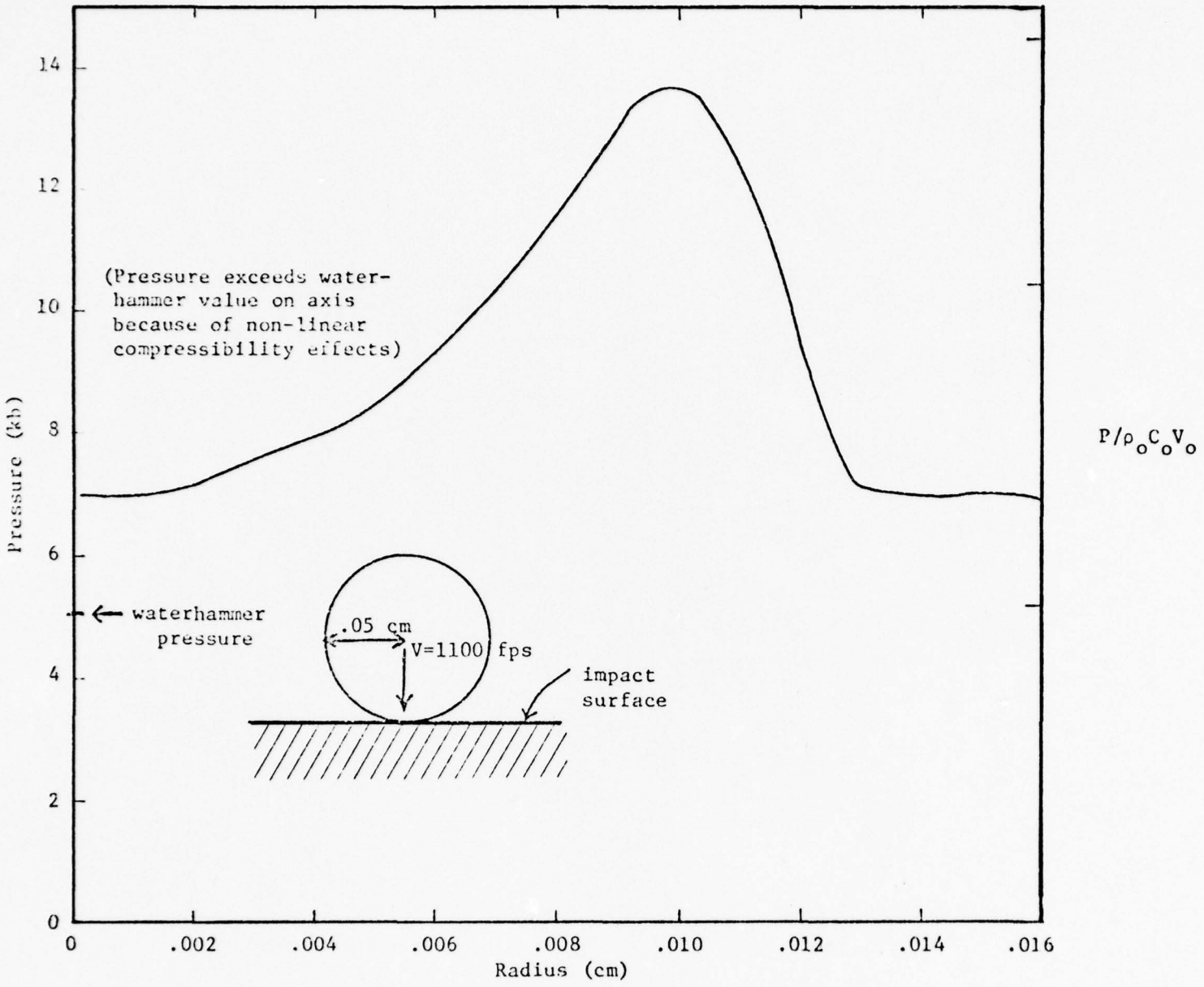

Figure 8. Peak Pressure on the Impact Surface Vs. Radius

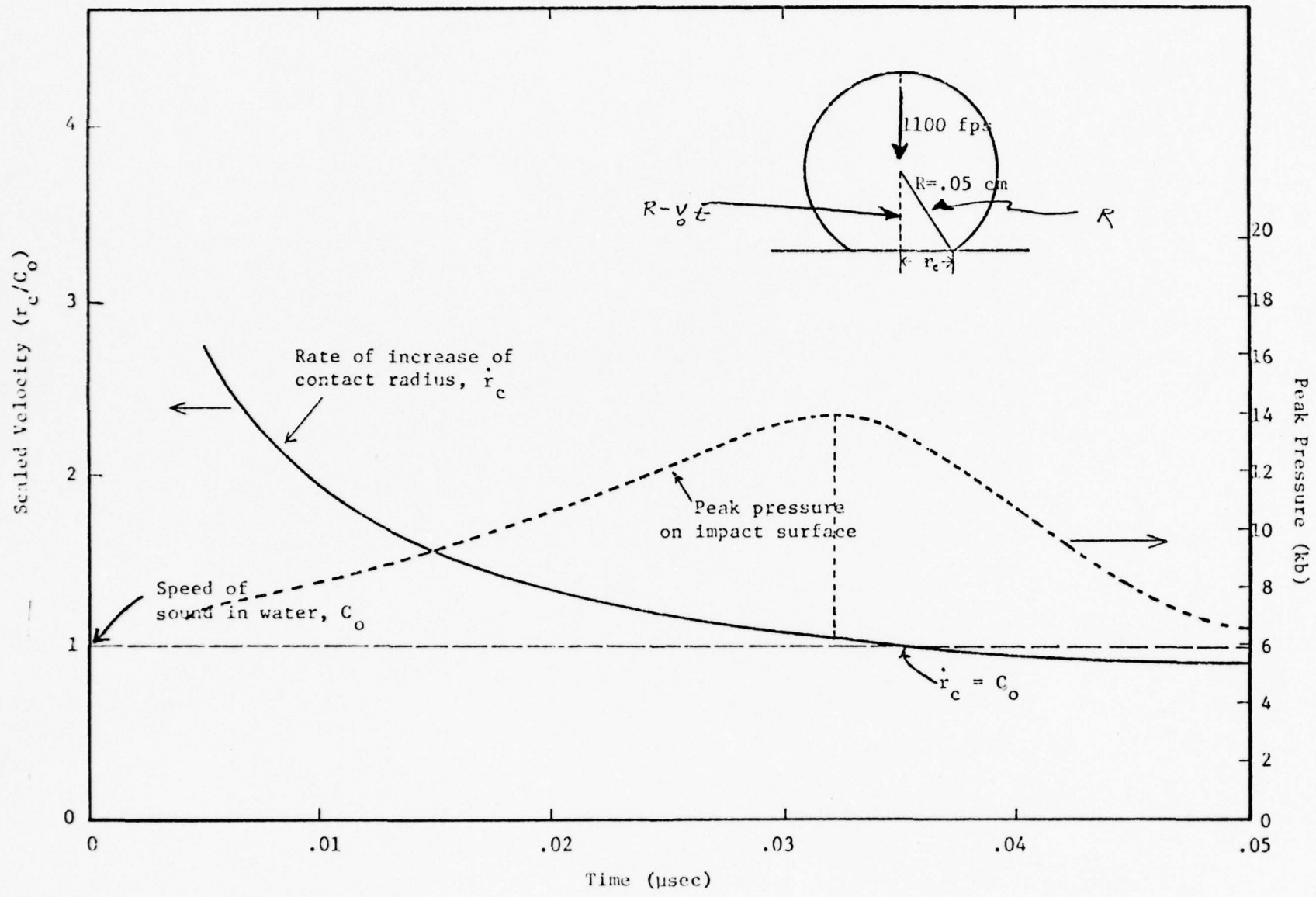

Figure 9. Rate of Increase of Impact Radius and Peak Pressure Vs. Time

$$r_c^2 + (R-V_o t)^2 = R^2$$

$$\therefore \dot{r}_c = \frac{V_o(R-V_o t)}{r_c}$$

The $\dot{r}_c$ versus time curve for the calculated case is plotted on Figure 9 as a solid line. Also shown on this curve is the speed of sound in undisturbed water (C_o) which is .15 cm/μsec or about 5000 ft/sec. The dashed curve shows the peak pressure versus time for this solution. The peak pressure attains its maximum at a time of about .033 μsec which corresponds to the time when the rate of increase of the contact radius ($\dot{r}_c$) nearly equals the speed of sound in undisturbed water. At times greater than .033 μsec, the peak pressure decreases.

Thus, we conclude that the peak pressure on or near the contact radius increases as long as the contact radius is increasing faster than the wave velocity in undisturbed water (C_o). Once the contact radius is traveling slower than this wave speed, then the pressure waves which interact with the water free surfaces generate relief waves which rapidly relieve the "excess" pressures (i.e., pressures exceeding the 1-D shock Hugoniot value) near the contact radius. By .05 μsec, for example, the peak pressure has been reduced from 14 kbar to 6 kbar. When the contact radius is moving faster than C_o but slower than the local shock velocity ($C_o < \dot{r}_c < C$), shock wave interactions with the droplet free surface is still possible. However, the compressive stresses generated by the impact of droplet materials on the rigid surface near the contact radius are sufficient to dominate any pressure relief from the shock wave interaction with the droplet free surface.

2.3 Discussion

The early experiments of Rochester and Brunton (Refs. 1, 2) indicated that the peak surface pressure during water drop impact probably occurred on the impact axis and were of the magnitude of $0.7\,\rho_o C_o V$. Cautions on this conclusion because of the large size of the pressure transducer were noted. Additional

refinement of experimental technique, including the development and use of smaller transducers led to the conclusion that the pressure of the center was still somewhat less than the waterhammer pressure, but that a maximum of 1.8 $\rho_o C_o V$ occurred at approximately .1 drop diameter off the impact center. In these experiments, the sizes of the pressure transducers were respectively approximately one-fifth and one-fifteenth of the drop diameter. The averaging over transducers of these sizes contributed to some uncertainty with regards to the physical location of the peak pressure pulse and its magnitude. The computed pressure pulse in Figure 6 is very sharp spatially and exhibits a maximum whose location is in good agreement with the more refined experimental data.

The response time of the transducer should also be considered in attempts to compare the present calculations with experiment. The experimental transducers were estimated to have a response time on the order of 0.1 and 0.2 microsecond. As indicated in Figure 7, the half width of the computed pressure transient during water drop impact is somewhat less than experimental response time of the transducer.

Combining the factors of physical size of the pressure transducers and the associated response time leads to the conclusion that the calculated maximum of 2.7 $\rho_o C_o V_o$ is not in disagreement with experimental limitations. Further substantiation of this experimental discretization effect was evidenced in earlier calculations performed with a coarser computational mesh. Careful interrogation of those results showed a pressure maximum occurring off-axis in a similar fashion. The computed magnitude of this pressure pulse was lower, about 1.6 $\rho_o C_o V$, and there was then uncertainty as to the validity of such narrow transients.

Examination of the pressure time distribution given in Figure 7 for the center of the impact leads to the impression that the present finely zoned calculations predict greater pressures than experimentally reported. However, if the relatively long experimental rise times for pressure transducers ($\sim$ 0.1 μsec) are taken into account, the appropriate time average of the present computations would not be inconsistent with the experimental observation.

The present studies provide guidelines for the formulation of experimental programs to refine the understanding of the impact pressures. If the present computations are representative of actual impact, then pressure transducers with fine spatial and temporal resolution are required. The discretization similarities between coarsely zoned computations and transducers of finite size should be recognized in experimental planning and interpretation of data. The results given in Figures 6 and 7 indicate that the transducers should be quite small (only a very few percent of the drop diameter) and the combined rise time of the transducer and instrumentation should be less than 0.01 μsec. The effects of spatial and temporal resolution could be simulated by time and space averaging of the present results, but such a process is outside the scope of the present study.

Heymann has cited several experimental results (Refs. 5, 6, 7) which would be consistent with his, and the present, prediction of a ring of off-axis pressure in excess of the one-dimensional waterhammer pressure. In common with the findings of Heymann and Rochester and Brunton, the zone of high impact pressure may be described as "localized and fleeting."

The relationship between the present pressure computations and localized material damage is addressed later. This division is deliberate as the physical principles governing material response such as crack or failure initiation and growth need not be invoked to describe the present results. What is of importance here is that fluid flow characteristics account for a pressure build-up phenomena of a different character than that associated with low speed solid impact, and may provide the mechanism of differing materials response between liquid and solid impact. Penetration of fluid flow into minute surface cracks would certainly be sensitive to the impact pressure distribution. This mechanism, for example, would have to be considered in evaluating materials response to the pressures developed during hydro-impact.

2.4 Summary

The present computations represent the most finely zoned hydrodynamic computation yet reported for liquid drop impact. These computations were specifically tailored to resolve the experimental and theoretical uncertainties associated with pressure distributions developed during hydrodynamic impingement. This objective was believed accomplished as evidenced by the well behaved flow fields obtained and the easy physical explanation of the computational results. It is concluded that significant highly transient pressure pulses exist off the impact center in general accordance with Rochester and Brunton's (Ref. 1, 2) experiments. The pressure peak occurs when the velocity of the radius of contact approximates the speed of sound in water. The basic nature of the phenomena appears general, and should be considered as a possible basis for differences between material damage mechanisms and/or observations for liquid and solid impact.

3.0 NUMERICAL CALCULATIONS OF AN 1100 FPS AND 4000 FPS IMPACT OF 290 MICRON GLASS SPHERES ON A ZnSe PLATE

3.1 Introduction

The numerical analysis of the dynamic velocity and stress fields resulting from the impact of glass spheres impacting elastic ZnSe was performed using a Lagragian finite difference code. A prime objective was to compare the dynamic results of this numerical analysis with the quasi-static results predicted by a Hertzian analysis. The purpose is to indicate the nature and significance of departures from the quasi-static model concepts commonly used in the literature.

The elastic projectile and target are divided into a number of volume elements, or cells, each of which has a set of stresses, velocities, etc., associated with it. The equations for updating the cell variables during a time cycle are obtained from the finite difference analogues of the conservation of mass, momentum, and energy equations along with the elastic constitutive relations for the materials involved. Table 1 indicates the elastic properties used in this study.

TABLE 1. ELASTIC PROPERTIES OF GLASS SPHERE AND ZnSe TARGET

	Density ρ_o (gm/cc)	Poisson's ν	Young's E (Mbar)
Glass Projectile	2.23	.2	.64
ZnSe Target	5.27	.3	.69

3.2 Results

Figure 10 shows the initial computational grid used for both the 1100 and 4000 fps cases. Figures 11, 12 and 13 show principal stresses (magnitude and direction) for the 1100 fps impact case at a time of .14 μsec. The plots roughly correspond to the time of maximum penetration. The Hertzian theory predicts a time of peak penetration of .15 μsec, while the dynamic solution predicted .13 μsec.

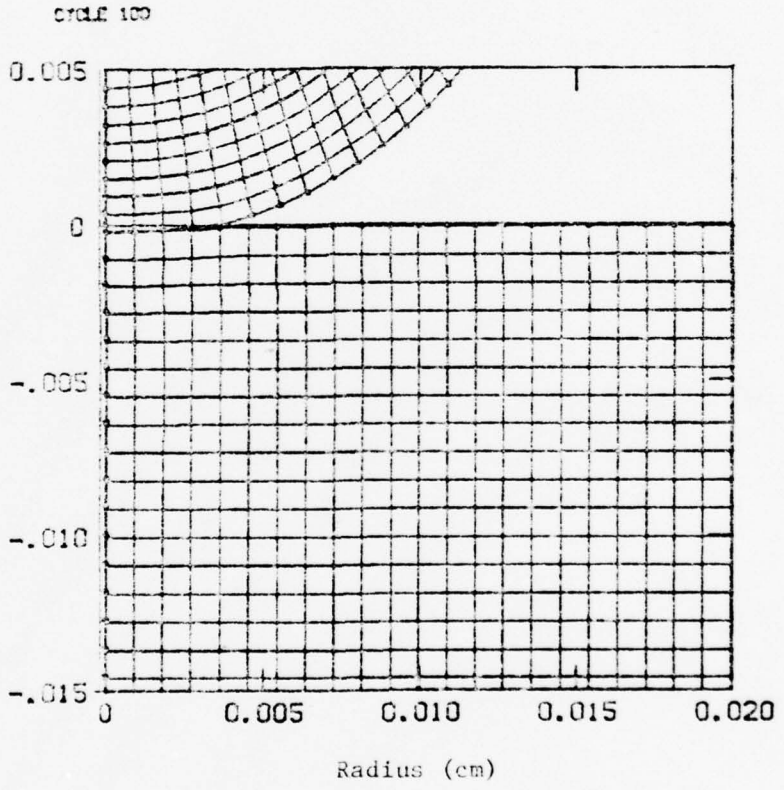

Figure 10. Computational Grid Near the Impact Point for the 1100 and 4000 fps Impacts of a 290 μ = .029 cm Glass Sphere on a ZnZe Target

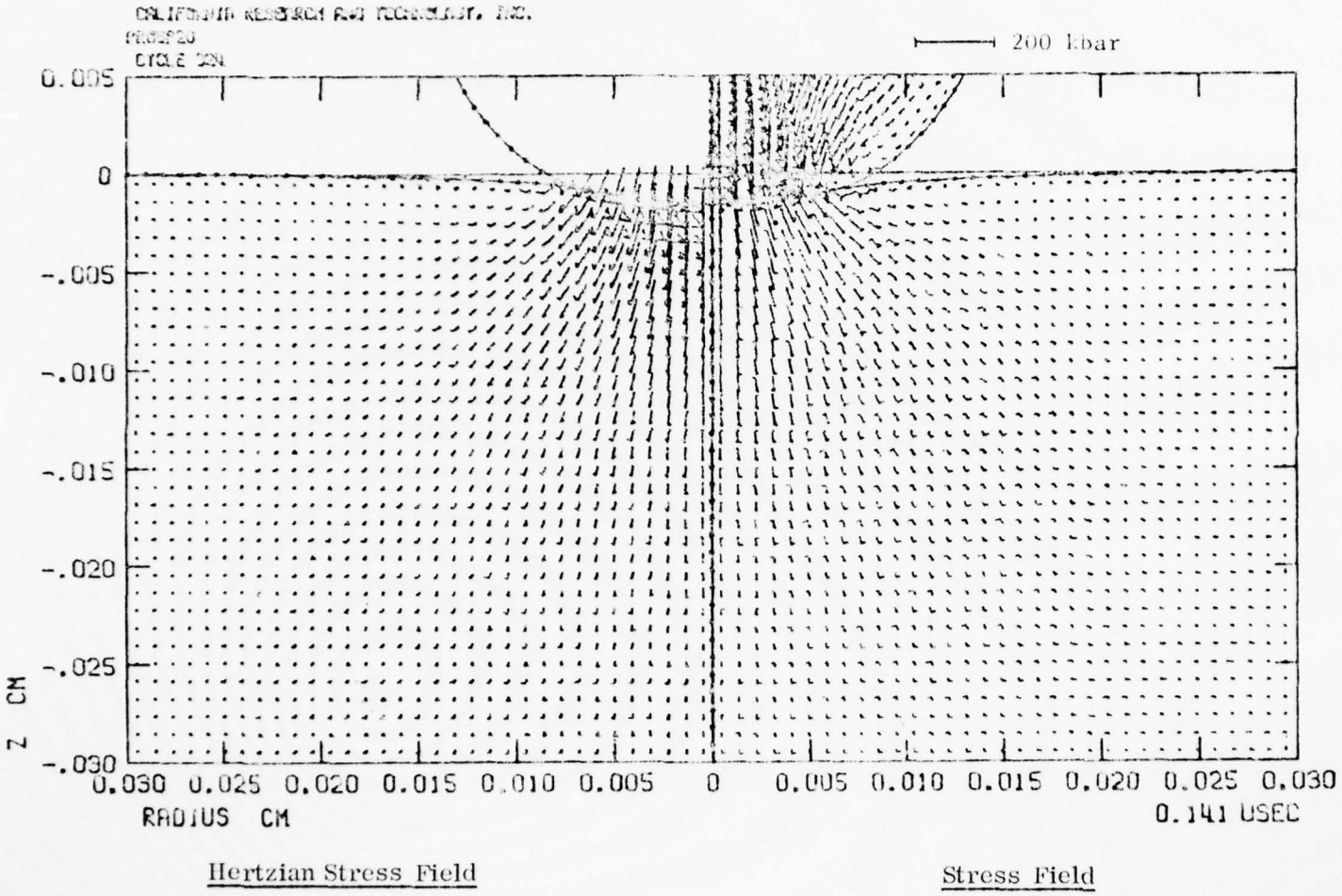

Figure 11. Comparison of the Stress Fields for the Dynamic Solution (V_s = 1100 fps), and for the Hertzian Approximation at .14 μsec ($T/T_p = 1.05$)

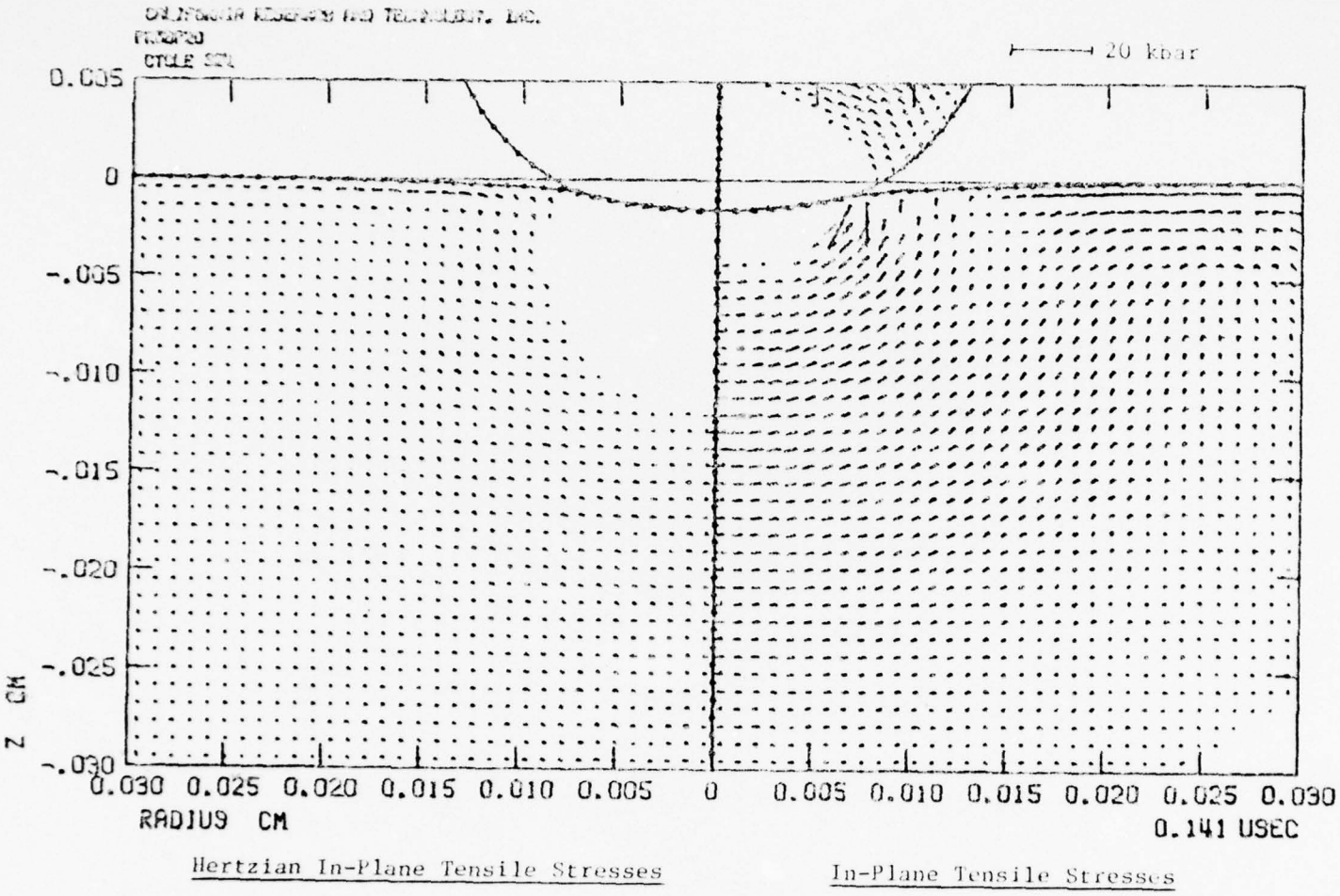

Figure 12. Comparison of the In-Plane Tensile Stresses for the Dynamic Solution (V_o - 1100 fps) and for the Hertzian Approximation at .14 μsec (T/T_p = 1.05)

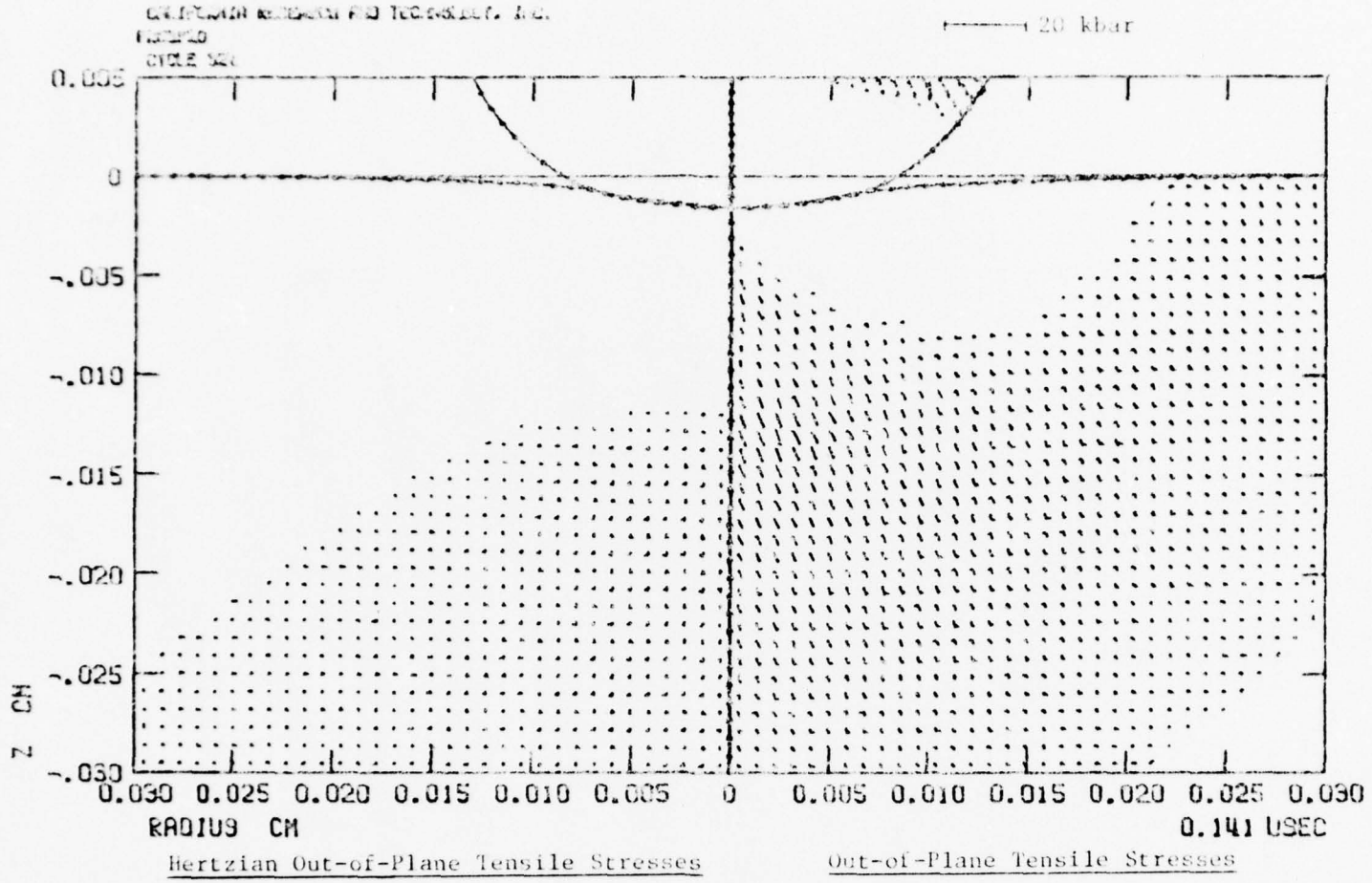

Figure 13. Comparison of the Out-of-Plane Tensile Stresses for the Dynamic Solution (1100 fps) and for the Hertzian Approximation at .14 μsec ($T/T_p = 1.05$)

Figure 11 is a comparison of the Hertzian stress field and the calculated stress field. The compressive stress fields are similar except near the projectile. As discussed below, the radial and hoop stresses are much lower in the dynamic calculation near the axis of symmetry. Note that there are no stresses in the projectile in the Hertzian case, whereas the dynamic calculation included the elastic projectile and the stress reflections and interactions between the projectile and deforming target surface. Figure 12 compares the tensile stresses in the r-z plane as predicted in the Hertzian quasi-static model with the numerically calculated in-plane tensile stresses. The dynamic tensile stresses are higher in magnitude and extend closer to the projectile as compared to the Hertzian case. Figure 13 compares the out-of-plane or hoop tensile stresses in the Hertzian versus dynamic case. The hoop tensile stresses are again larger and again extends closer to the penetrator. Also, note that hoop tensions exist in the dynamic case at the target front surface about two radii from the axis of symmetry. In the Hertzian quasi-static solution, no hoop tensions develop near the surface. We therefore conclude that the dynamic solution represents a much more severe tensile environment than does the Hertzian solution.

Figures 14, 15, and 16 show comparisons for the 1100 fps case of the components of the stress tensor near the target surface at three times. Figures 17 through 22 show the same stress comparisons at the time of peak penetration for the 4000 fps case. Also on these plots are a comparison with the predictions of the Hertzian theory. The agreement with respect to the axial stress (σ_{zz}) is good. This agreement is responsible for the good comparison of time to peak penetration depth and actual penetration between the calculations and Hertzian theory. Table 2 summarizes these comparisons. The radial and hoop components of stress (σ_{rr} and $\sigma_{\theta\theta}$), however, have a distinctly different character in the dynamic solution as compared to the Hertzian theory. The differences concern the behavior directly under the projectile. The Hertzian theory predicts a peak compressive radial and hoop stress near the axis, while the dynamic solution shows the radial and hoop stresses approaching zero stress near the axis of cylindrical symmetry. This difference is due to the

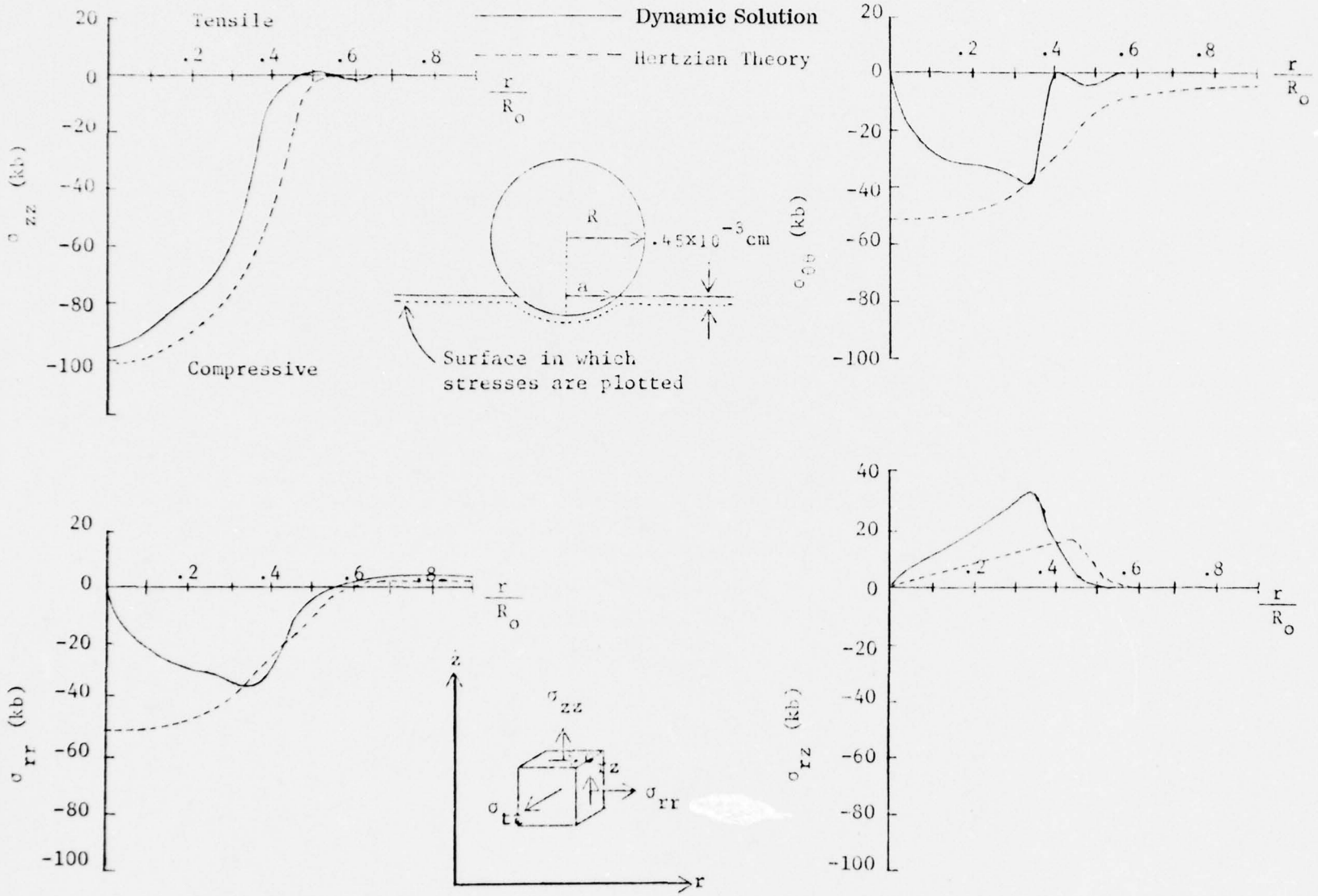

Figure 14. Stress Field Along the Surface of the ZnSe Plate at .06 μsec ($T/T_p = .46$) for the Dynamic Solution (1100 fps) and for a Hertzian Impact

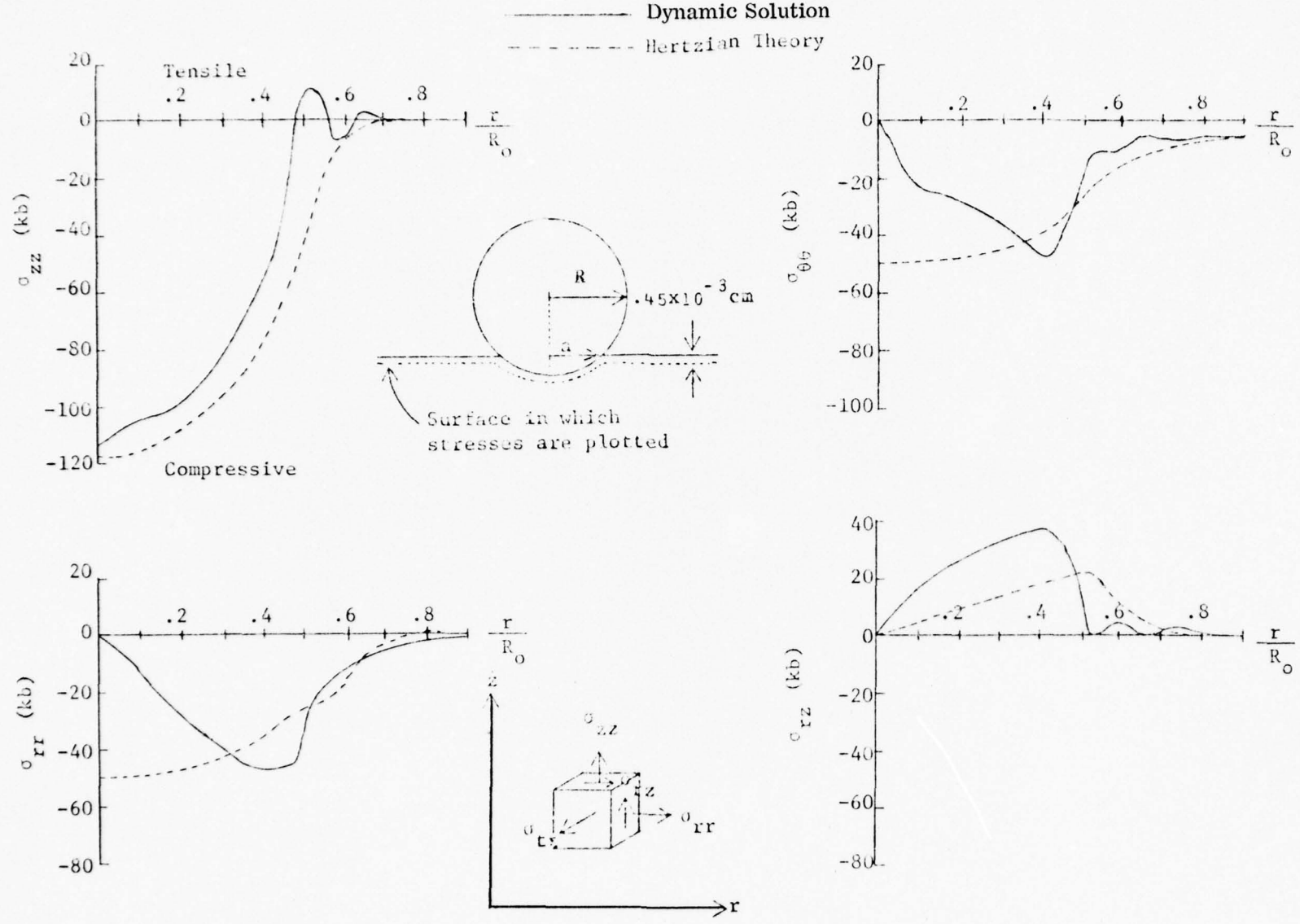

Figure 15. Stress Field Along the Surface of the ZnSe Plate at .14 μsec (T/T_p = 1.05) for the Dynamic Solution (1100 fps) and for a Hertzian Impact

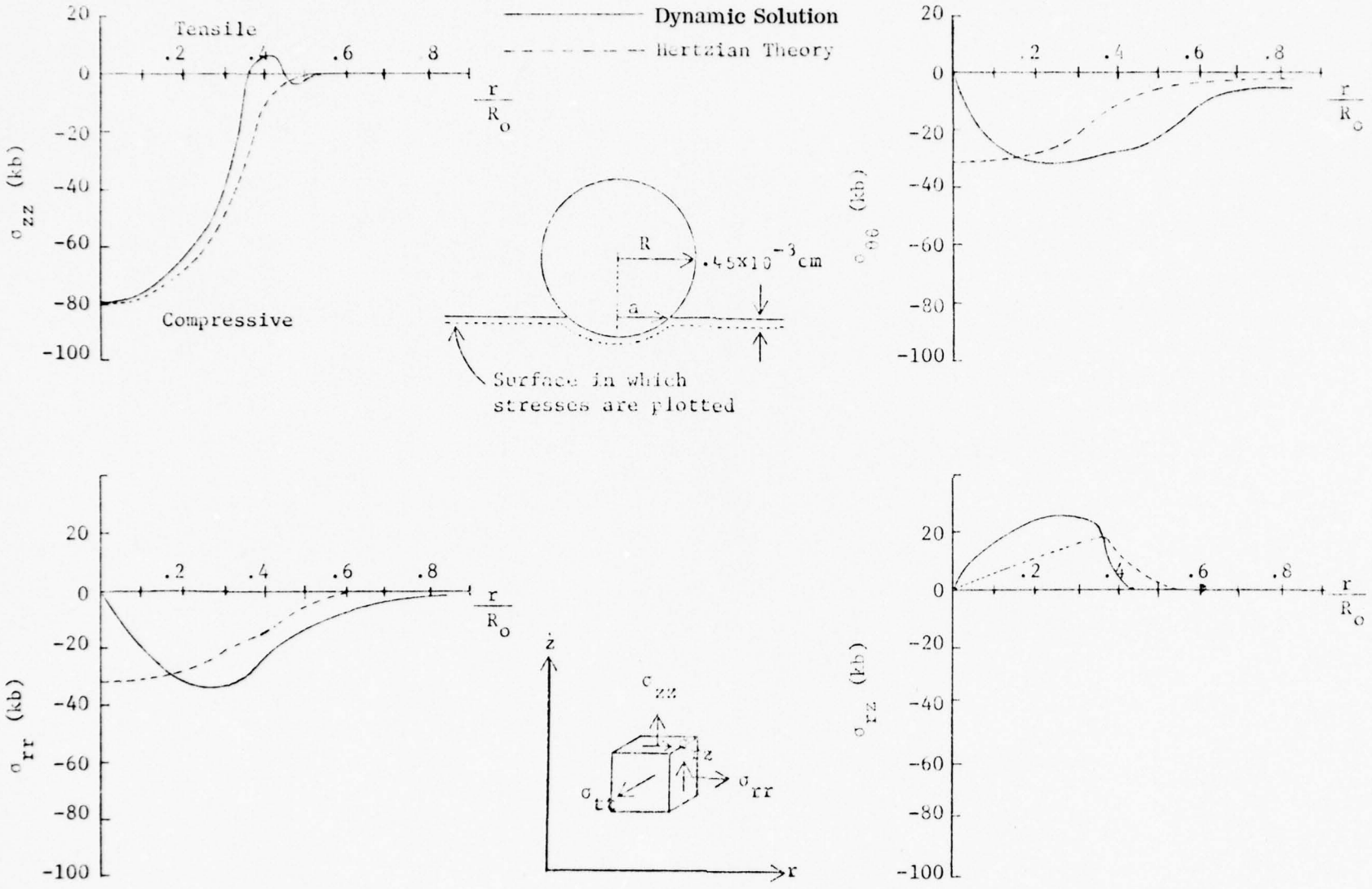

Figure 16. Stress Field Along the Surface of the ZnSe Plate at .22 μsec ($T/T_p = 1.6$) for the Dynamic Solution (1100 fps) and for a Hertzian Impact

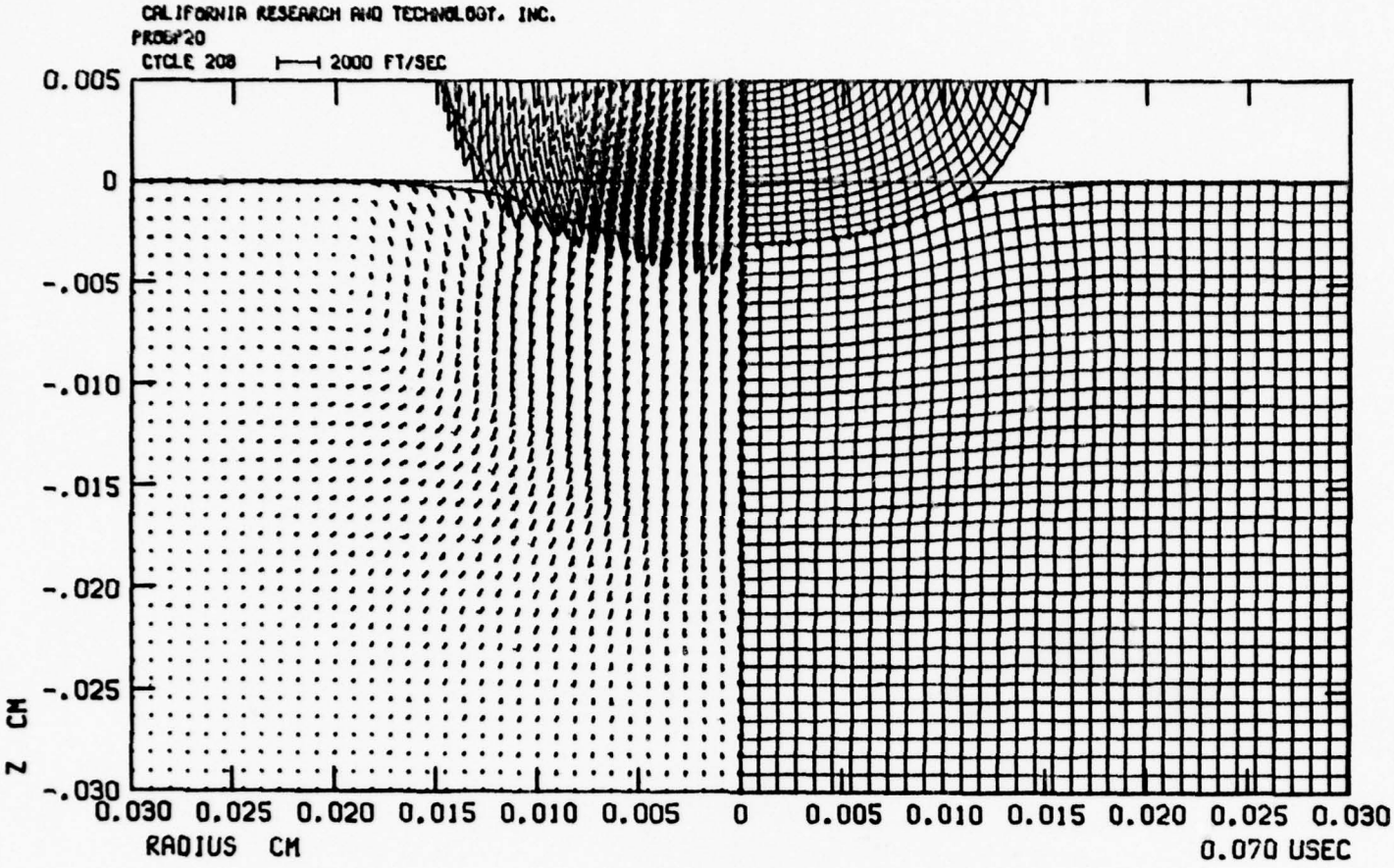

Figure 17. Velocity Field and Computational Guide for 4000 fps Solution at .07 μsec

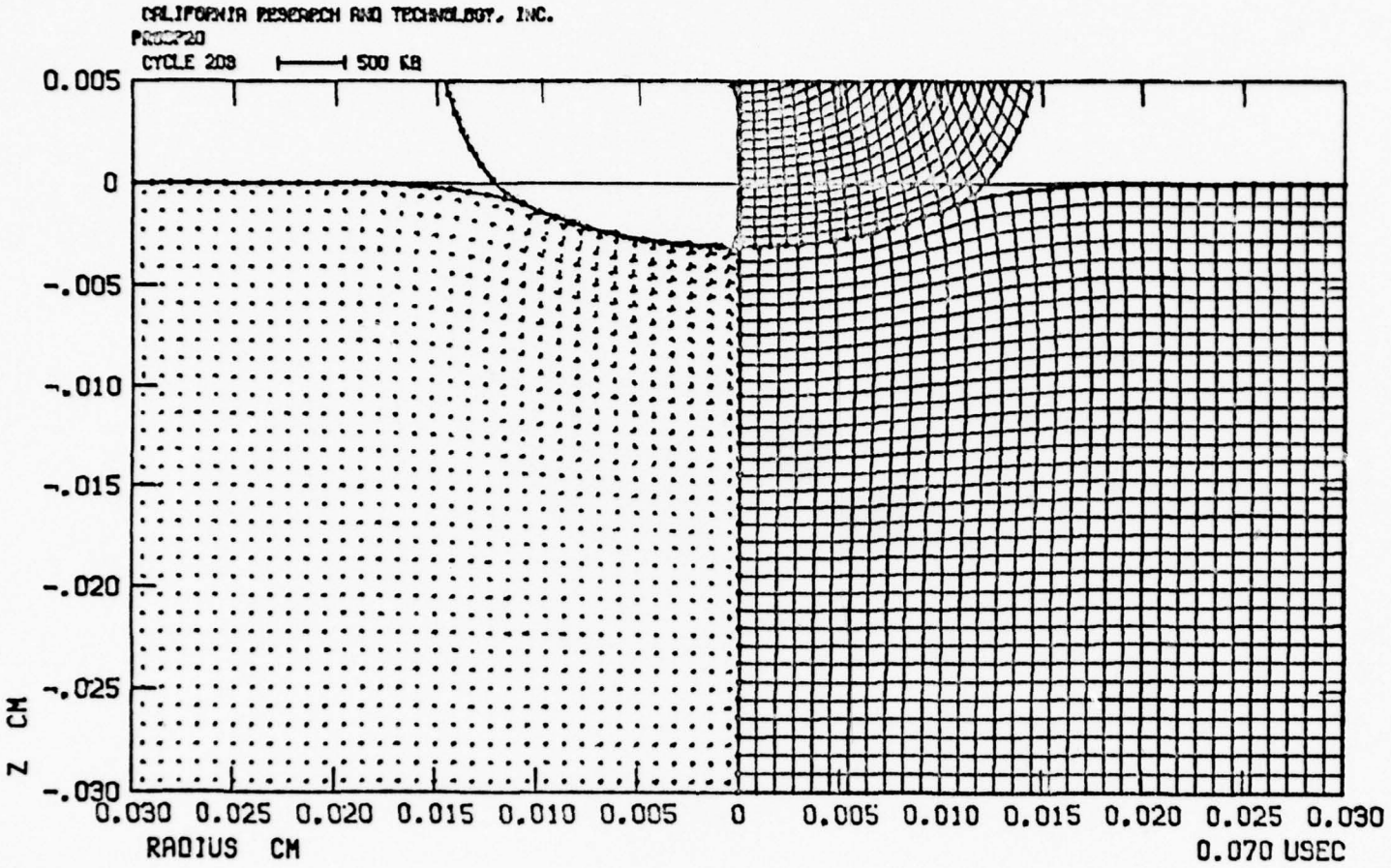

Figure 18. Stress Field in ZnSe Plate for 4000 fps Less Hertzian Stress Field at .07 μsec

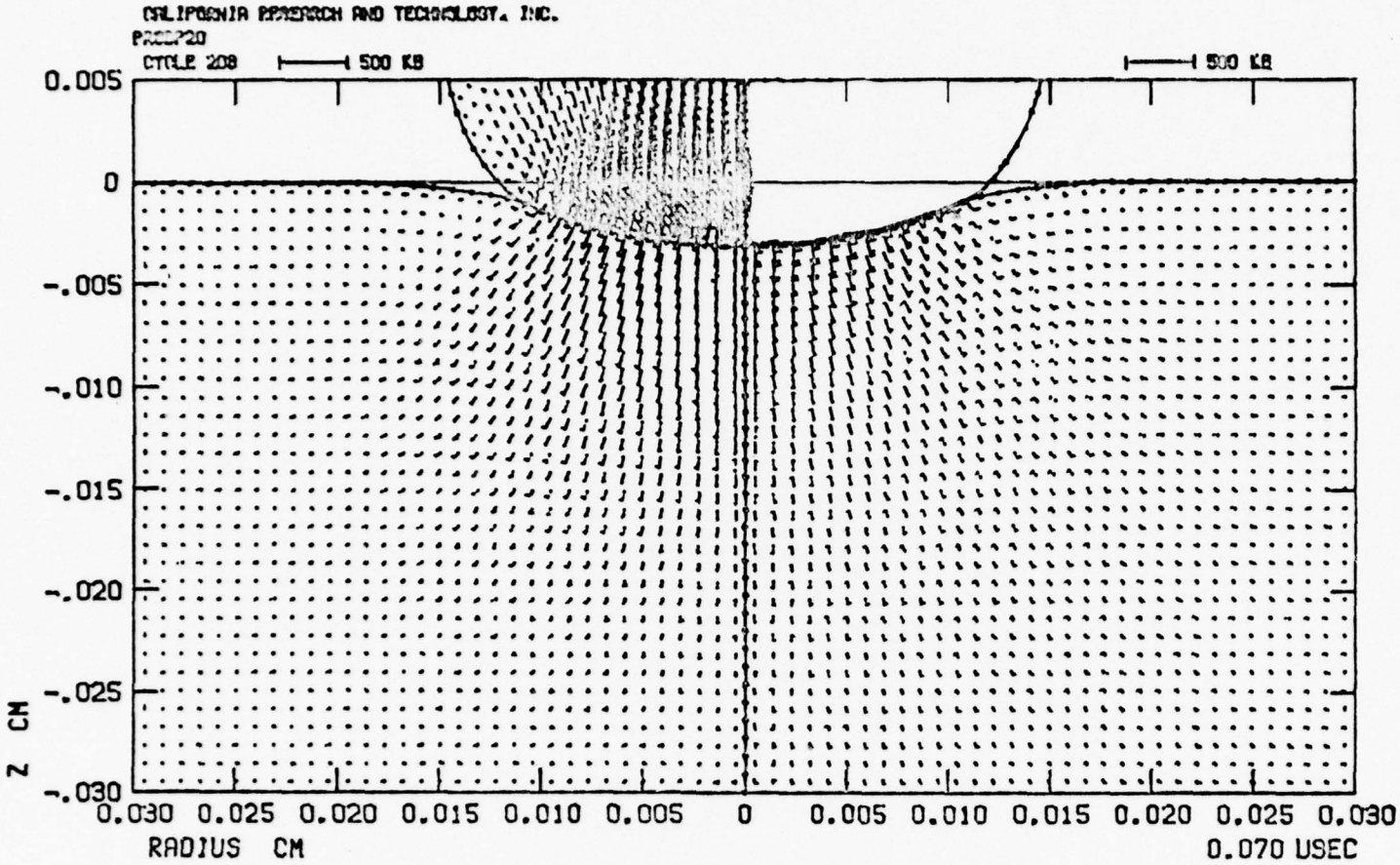

Stress Field

Hertzian Stress Field

Figure 19. Comparison of the Stress Fields for 4000 fps Solution and for the Hertzian Approximation at .07 μsec

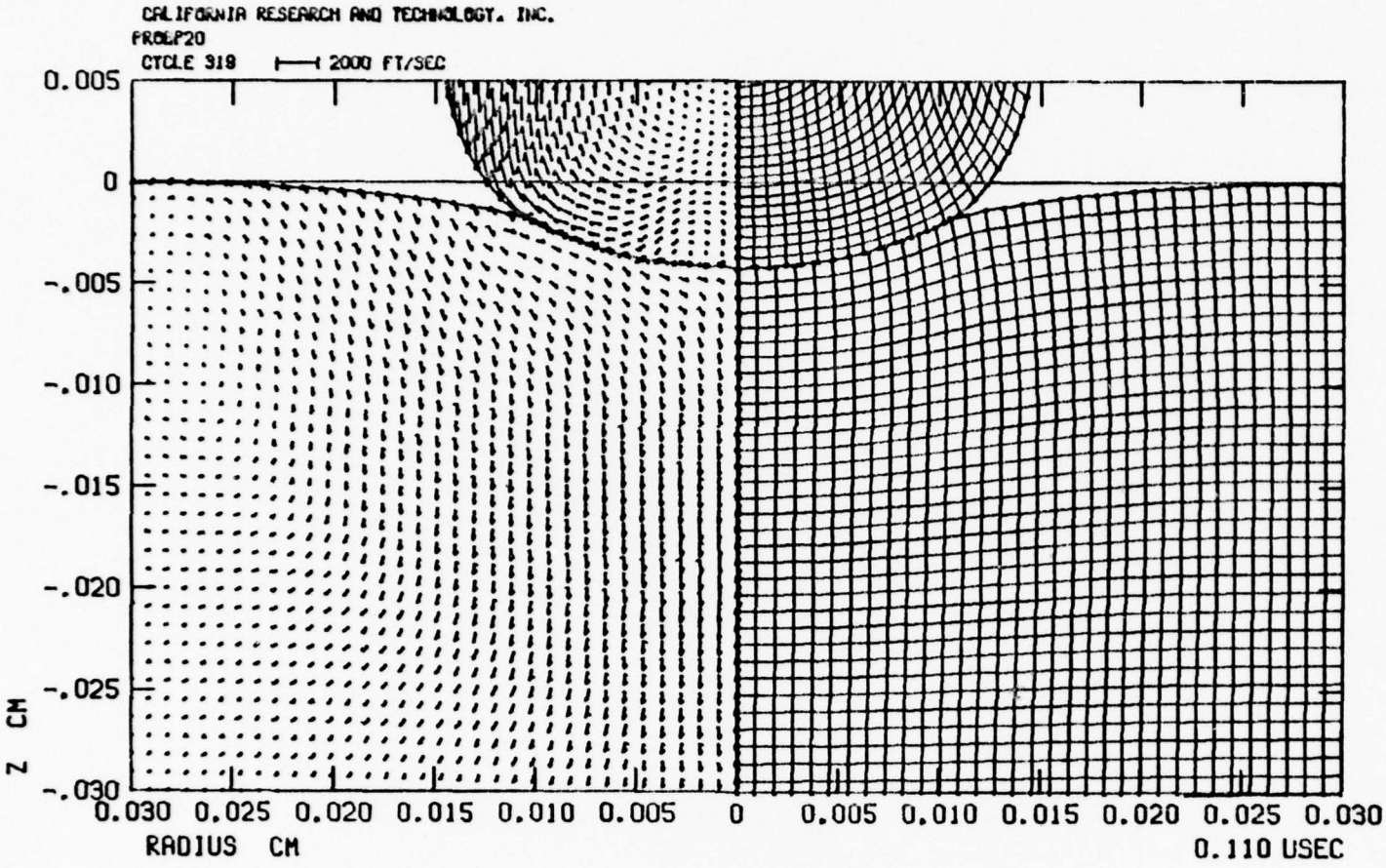

Figure 20. Velocity Field and Computational Grid for 4000 fps Solution at . 11 μsec

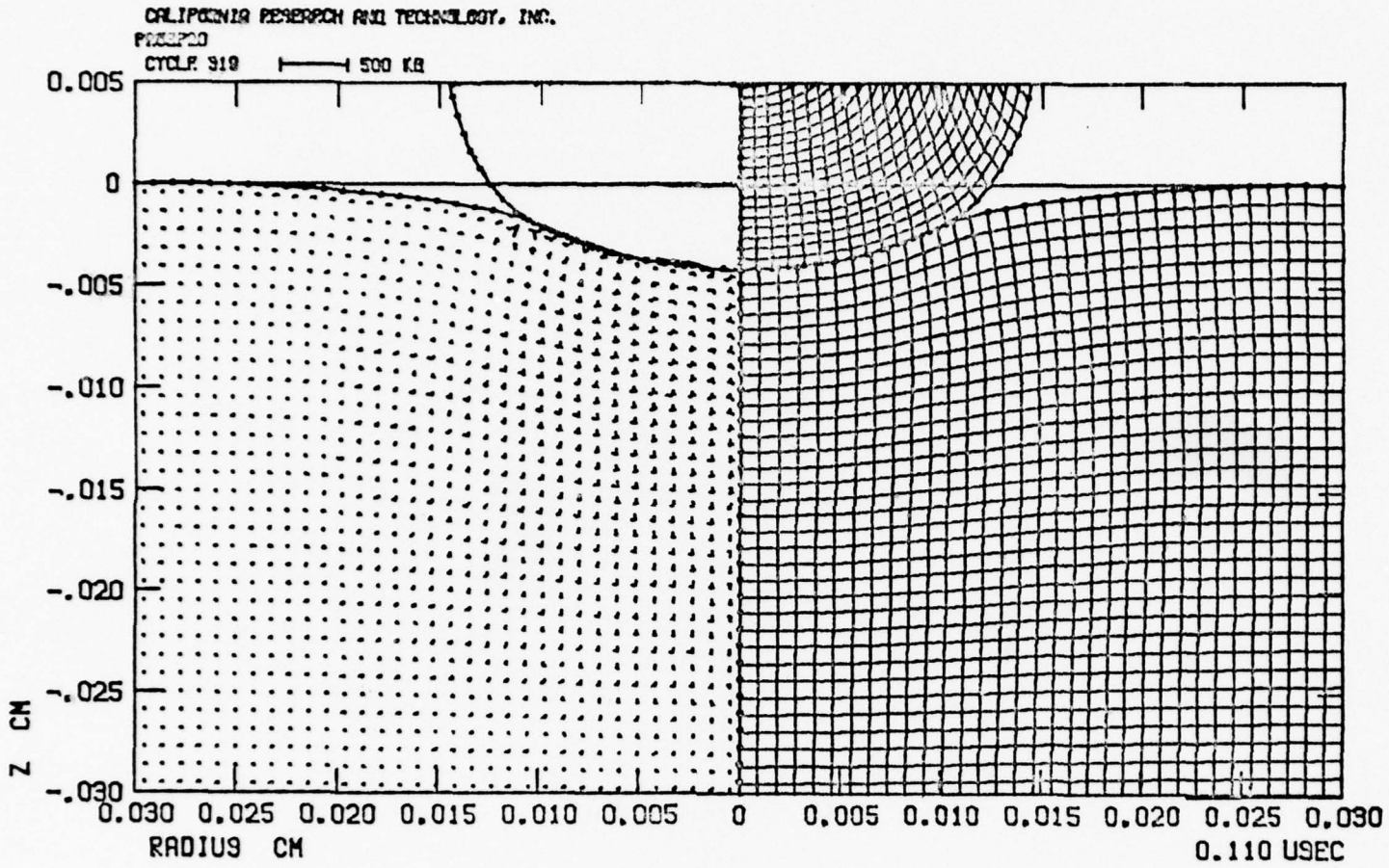

Figure 21. Stress Field in ZnSe Plate for 4000 fps Solution
Less Hertzian Stress Field at .11 μsec

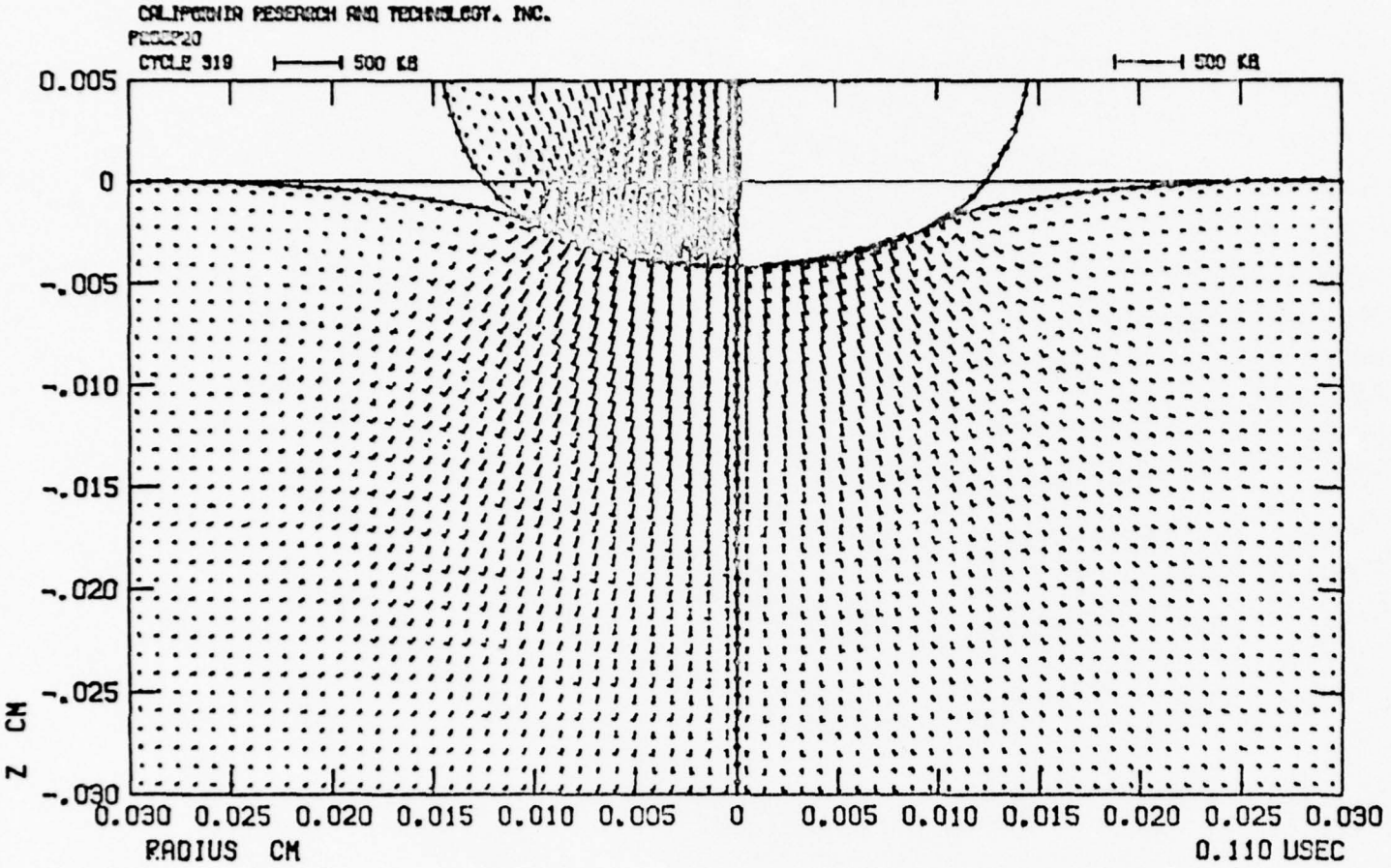

Stress Field

Hertzian Stress Field

Figure 22. Comparison of the Stress Fields for 4000 fps Solution and for the Hertzian Approximation at .11 μsec

TABLE 2. COMPARISON BETWEEN DYNAMIC SOLUTION AND HERTZIAN THEORY

	Dynamic Solution	Quasi-static Hertzian Theory
Peak Normalized Contact Radius A_{max}/R	.55	.49
Peak Normalized Penetration, α_{max}/R	.21	.24
Time of Peak Contact Radius, T_p	.13 μsec	.15 μsec

deformation of the target front surface caused by the spherical penetrator. This deformation is realistically treated in the dynamic calculations, but ignored in the small displacement Hertzian theory.

3.3 Discussion

The calculated results of a Mach 1 impact of a 290μ glass bead on a ZnSe target were examined in detail. The impact conditions were chosen to complement previous studies performed by Ca. R. T. for AFML. The major differences are the diameter of the impacting particle, and the suppression of the fracture conditions within the target. In other words, this is the dynamic equivalent of the Hertz impact simulation.

There are several levels of comparison to consider. First, consider the indentation parameters of maximum penetration, radius of contact, and arrest time (or time of maximum penetration) for the particle (Table 2). Nothing blatently different is evident. In fact, from this point of view, one is tempted to conclude that at Mach 1, the Hertz model does quite well. This has been found to be a premature conclusion.

The differences in Table 2 can be very easily rationalized. The larger contact radius of the dynamic problem is to be expected because of the large deformations at the point of impact. As is true of many linear elasticity problems, the Hertz boundary conditions are satisfied with the implicit notion of small displacements. A sphere indented to about one-fourth of its radius results in large deformations of the target and sphere so one should expect the contact radius to be larger than that calculated for the Hertz model. Because of this larger pressure bearing area, one should expect the maximum penetration calculated by the dynamic WAVE-L method to be somewhat smaller. Of course, granted the above two considerations, the natural conclusion is that the time needed to bring the impacting sphere to rest should be somewhat shorter because of the smaller penetration. All of the above are consistent with the WAVE-L versus Hertzian comparison.

The comparison of the surface pressures (Figure 23) reveals additional reasonable correlation consistent with the above. So far, then, the Hertz simulation does not look bad even for Mach 1 impact.

If the principal stresses are compared for times approximately half way to maximum and maximum indentation (Figures 24 and 25), not much strikes the eye. Closer inspection reveals that excepting the compressive wave propagation phenomena, the hoop or circumferential direction stresses are the major visible differences.

These comparisons do not, however, tell the correct story as to the behavior of materials under impact conditions. The figures are scaled by the compressive stresses which are much larger than any tensions developed. The material response of cracking and degradation of transmission is dominated by the in-plane tensions, and the tension comparison is the correct one for evaluating the applicability of the Hertz model, not the compression dominated indentation parameters.

The comparison is striking (Figures 26 and 27). In these figures, compression is suppressed from plotting and stress scaling for explicit comparison of tensions has been performed. Not a lot of differences are noted for stresses developed

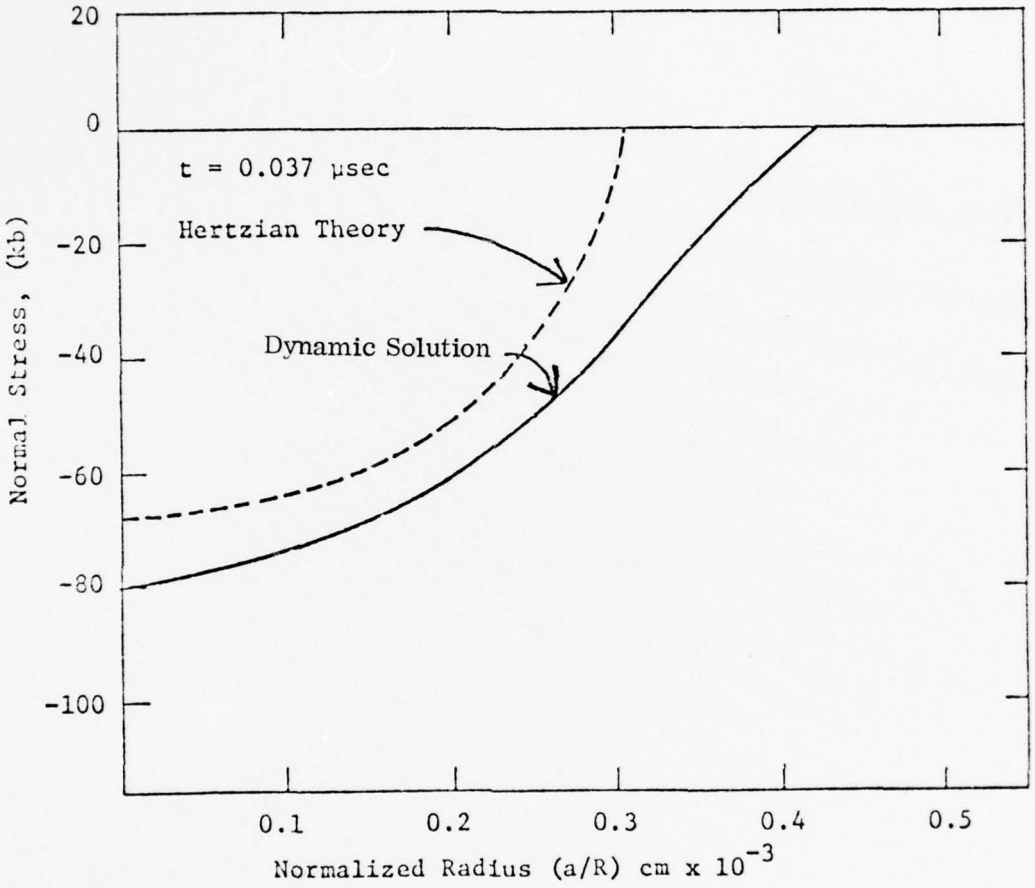

Figure 23. Stress Normal to Indentor Versus Radius at 0.037 μsec for Dynamic Solution and Accroding to Hertizian Theory

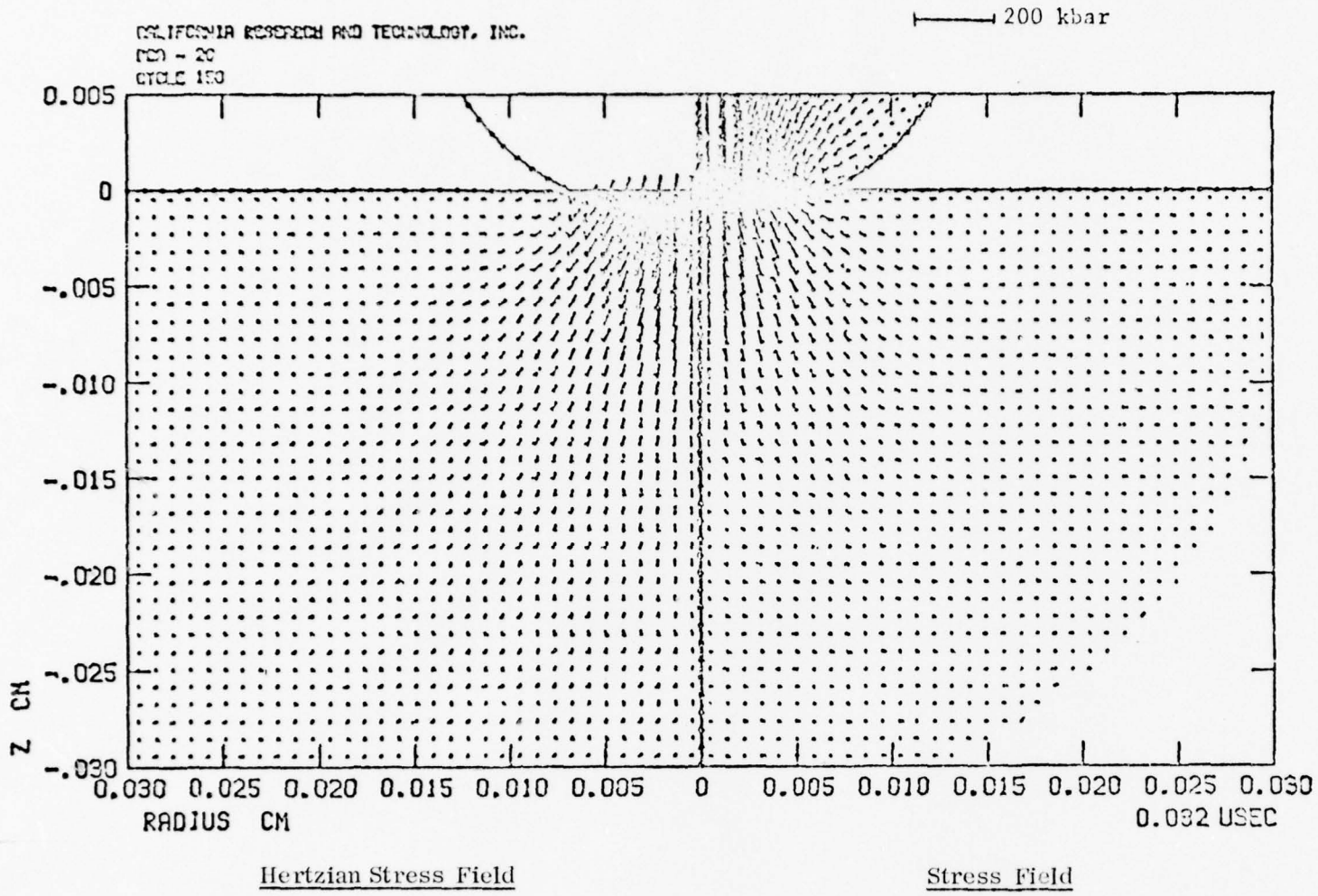

Figure 24. Comparison of the Calculated Stress Fields and the Hertzian Approximation at .062 μsec ($T/T_p = .46$)

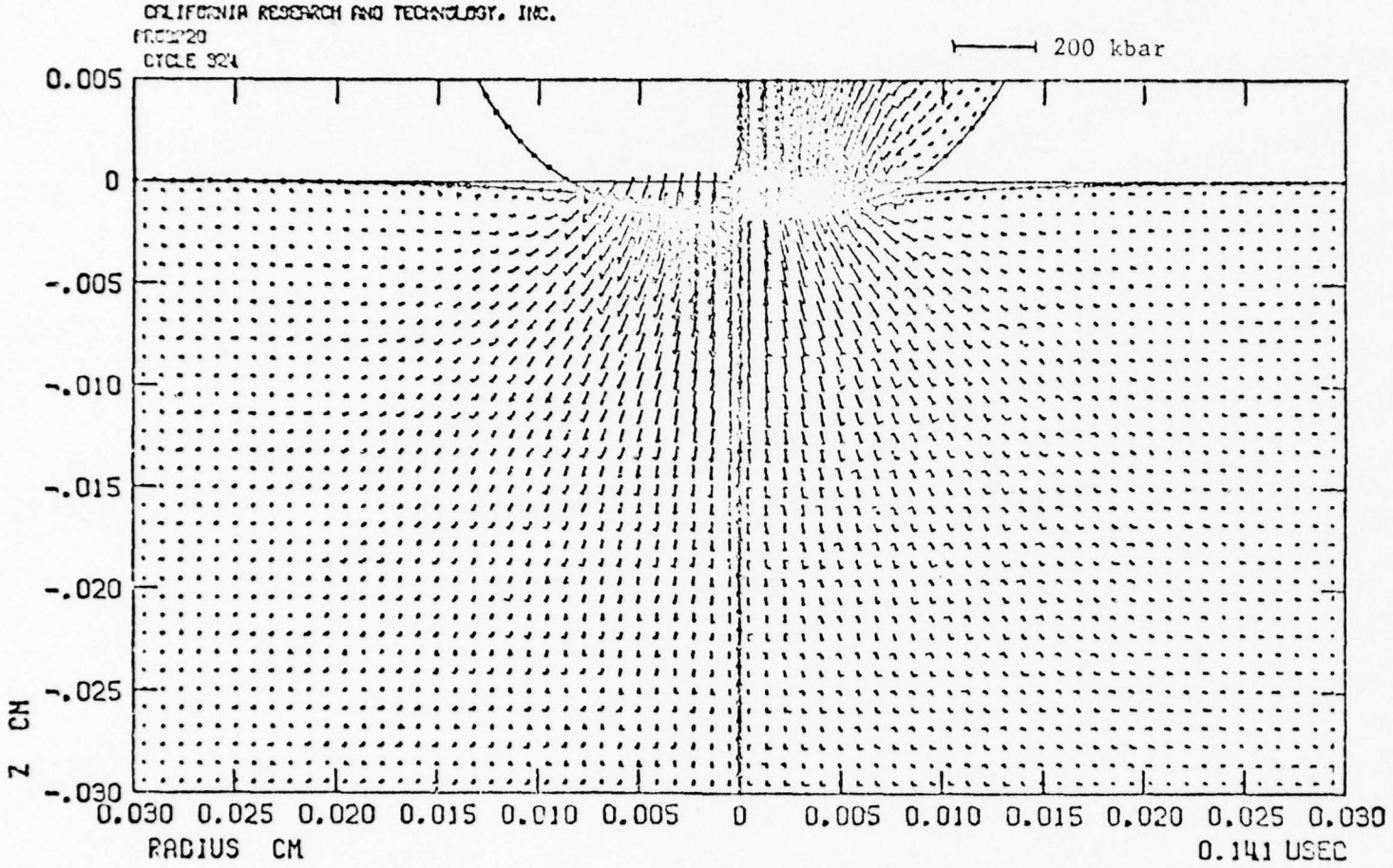

Hertzian Stress Field

Stress Field

Figure 25. Comparison of the Calculated Stress Fields and for the Hertzian Approximation at .14 μsec ($T/T_p = 1.1$)

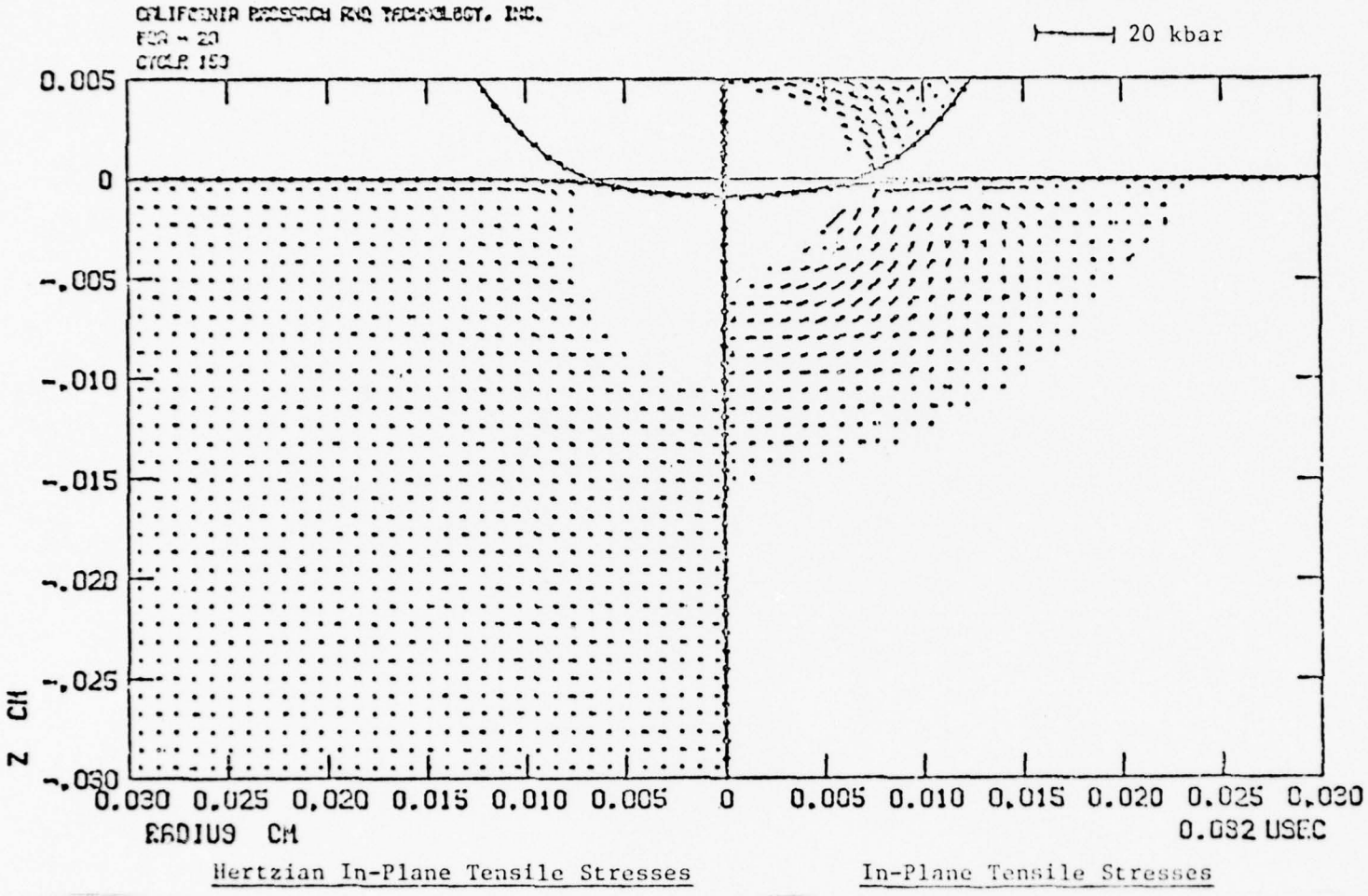

Figure 26. Comparison of the In-Plane Tensile Stresses and for the Hertzian Approximation at .062 μsec ($T/T_p = .46$)

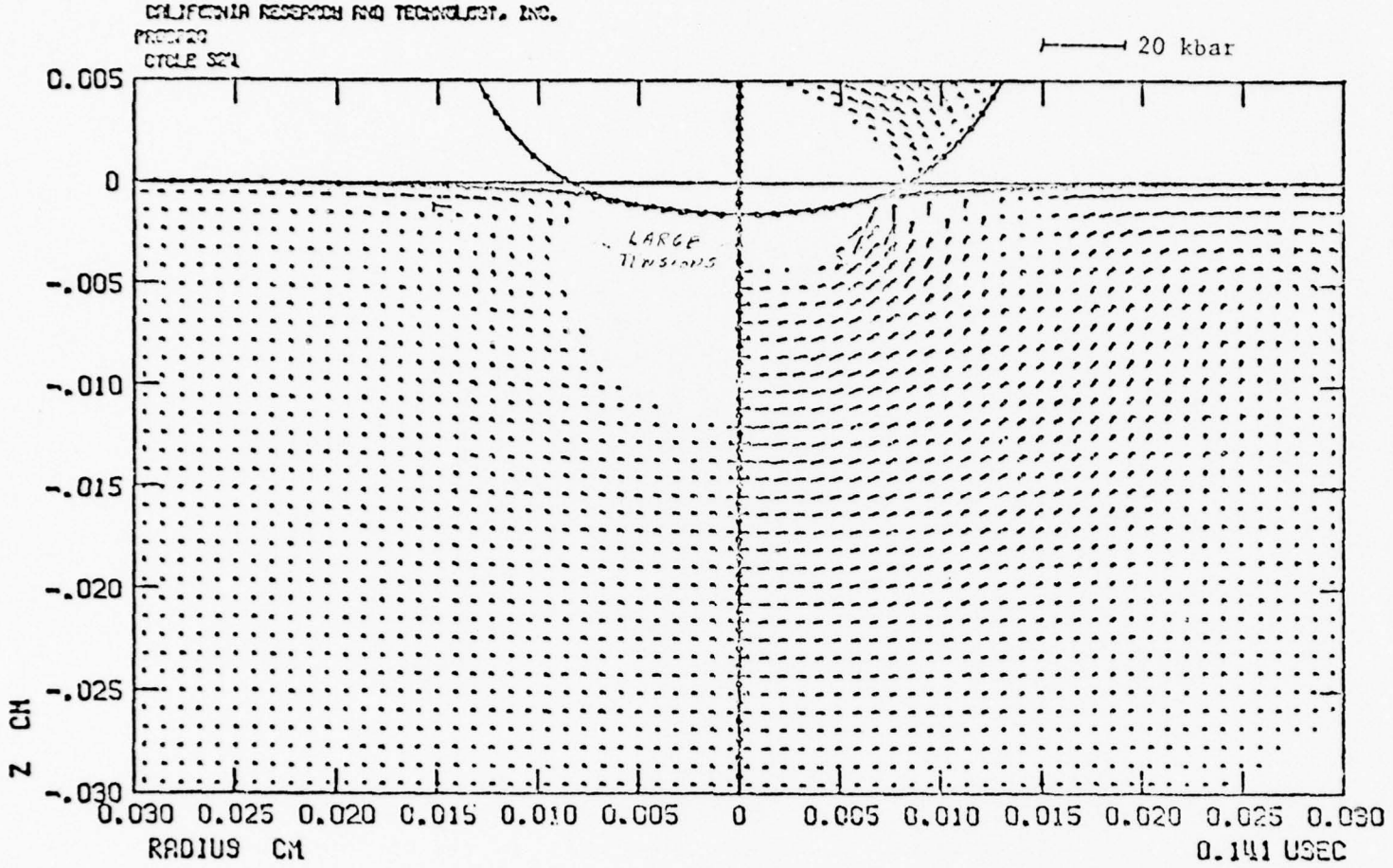

Figure Comparison of the In-Plane Tensile Stresses and for the Hertzian Approximation at .14 μsec ($T/T_p = 1.1$)

at the surface. However, very large differences are noted in the interior of the target. Probably the most significant aspect of this is that even if fracture initiation of the free surface could be suppressed by surface treatments such as etching or even thin coatings sized taking into account the rapid fall-off of radial tensile stresses with depth intrinsic to the static Hertz model, the subsurface tensions which are revealed in the dynamic problem will contribute to cracking and degradation of optical response if not outright fracture.

Before accepting this conclusion, however, one should capsulize the reasons for the dynamic versus static analysis disparity. The first clue is its relation to a wave which moves slower than the compressive (i.e., "p") wave, in other words the shear or "s" wave. Shear is, after all, identical to equal and mutually perpendicular tension and compression.

The simple diagram in Figure 28 extracts the basic mechanical phenomena of interest. The axisymmetric pressure distribution is replaced by symmetric (axisymmetric if you like) point loads (step loading with time to be more precise). The p and s waves propagate as shown and the sign of the shears developed is shown. The situation at a later time is indicated in Figure 29. An essential feature is that as the shear waves approach the axis of symmetry, they have opposite signs. On the axis of symmetry, they will superimpose and cancel. Off the axis of symmetry, zones can be defined in which no superposition has occurred (i.e., only one "s" wave has passed the point) as well as regions in which superposition but incomplete cancellation has occurred (i.e., points through which both "s" waves have passed but because they have traveled unequal distances from their origins, the wave front strengths are unequal due to inverse power law attenuation effects).

The result of this wave front propagation is that in general there will be zones in which shear stresses do not reflect the static symmetry, and are higher than the static solution. Since shear is a combination of tension and compression, the dynamic in-plane tensions are substantially higher than the static solution.

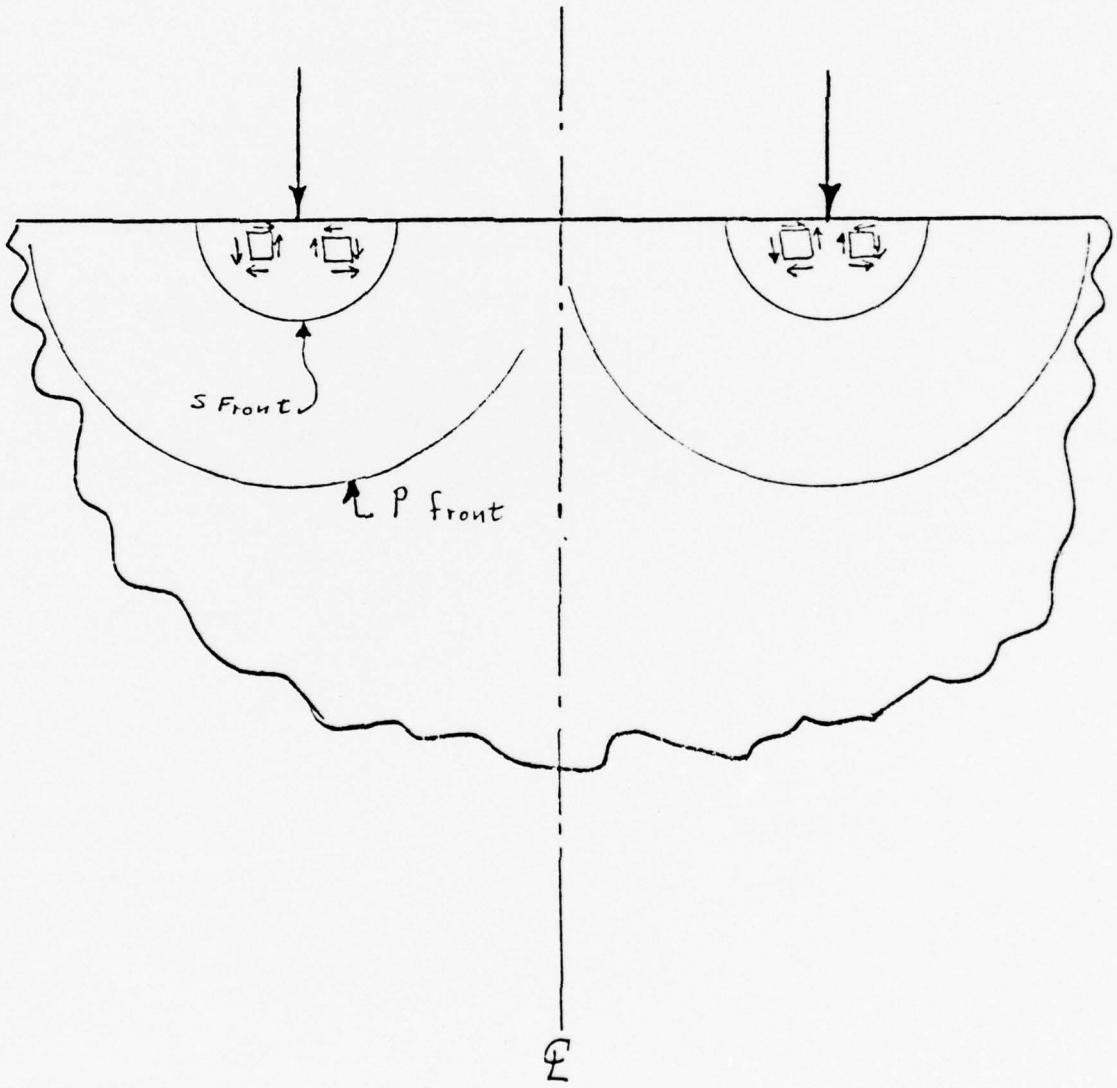

Figure 28. Two Point Loads

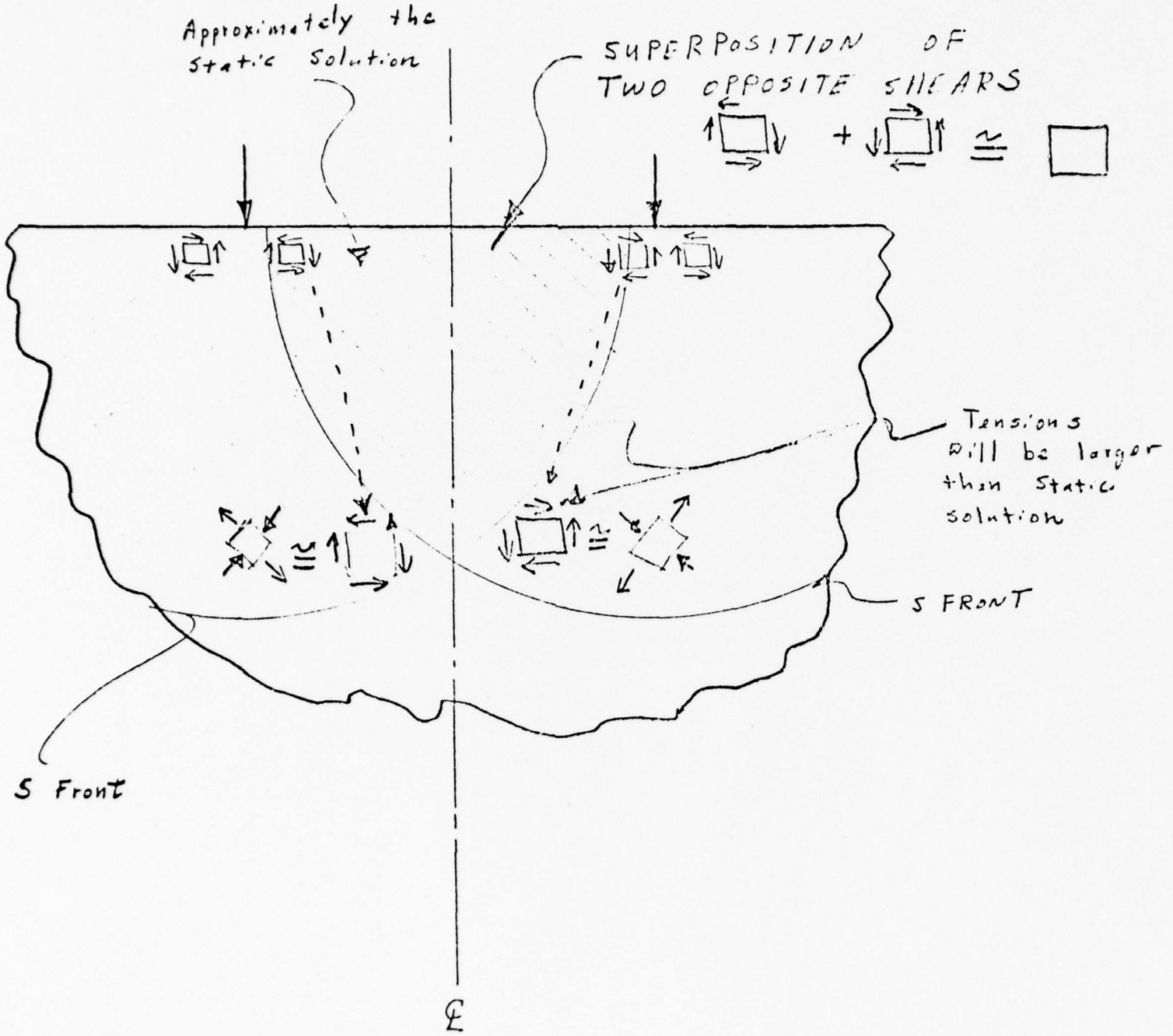

Figure 29. Superposition of Shear Fronts

4.0 CRACK NUCLEATION AND GROWTH FROM LOW VELOCITY PARTICLE IMPACT ON BRITTLE MATERIALS

4.1 Introduction

For low velocity impact of solid spherical particles, the quasi-static Hertz model well describes the stress state and deformation associated with maximum indentation. There are general correlations between the Hertzian tensile stresses for a variety of impact conditions, the material tensile strength and tensile strength statistics, and the observation of cracking and/or mass loss. There are also a variety of correlations between fatigue behavior and the multiple impact mass loss and cracking behavior.

The purpose of this task is to present a basis for the prediction of the combined effects of crack nucleation and growth, and to apply this formalism to liquid and solid impact data. The basic working hypothesis is that the probability of observing a crack as a result of impact is equal to the joint probability that a crack was initiated (or a crack source was activated) and the probability of growth to a size or geometry which is experimentally detectable (e.g., direct microscopy or fracture strength reduction).

4.2 Background

The two basic concepts to be used are probabilities of activation of crack sources and probabilities of crack growth. These will be illustrated in the following discussions.

Activation of crack sources was, perhaps, first discussed by Griffith in terms of the unstable propagation of pre-existing cracks. Basically, this work consisted of careful delineation of the crack tip stress state and/or gross energy balances for the system as a function of crack size and applied stress. The conditions for crack growth were definable as either the exceedance of a local crack tip stress state, or of a crack tip strain energy release rate. The instability resulted from the fact that once this condition was met or exceeded, further crack growth would guarantee that the condition would still be exceeded. Time was not an explicit field variable.

Weibull applied the concept of "weakest-link" to the fracture of solids to describe the mean value strength, the strength statistics, and strength increases for small stressed regions. This concept is more of a mathematical statistical model than a physical one. The weak links are described by convenient mathematical distribution functions and parameters which allow the fitting of statistics of fracture (as well as a host of other data not involving the weakest link postulate).

Fisher and Holman introduced the concept of flaw size and orientation distributions, which when coupled to the Griffith relationship, provided a statistical failure criterion explicitly coupled to flaw characteristics. This approach also predicted a strength versus size relationship through the weak-link postulate that the failure probability was equal to the probability of propagation of one or more cracks. In common with the Griffith and Weibull approaches, explicit considerations of crack growth kinetics were taken into account.

The early studies of crack growth related to impact phenomena were associated with attempts to define the "equations of motion" for a crack in a continuum. In addition, studies have been conducted from an atomistic or statistical mechanics point of view. Some of these methods also introduce explicit considerations of microstructure.

It is probably fair to comment that the problem of the kinetics of crack propagation is very complex, and that much additional work is required in this area. Fatigue behavior is probably in a similar status. Short term objectives for progress in these areas are the development and application of empirical correlations of laboratory studies.

Some success has been attained in correlating crack propagation studies with the stress intensity concept; i.e., the character of the elastic stress state near the crack tip. For slow crack propagation, the following empirical relationships have been found useful.

$$\frac{da}{dt} = f(\sigma\sqrt{a}) = f(k)$$

where

$k = \sigma\sqrt{a}$ = index of crack tip stress intensity

σ = applied stress field

a = crack size

and common forms are

$$\frac{da}{dt} = A(\sigma\sqrt{a})^n$$

or

$$\frac{da}{dt} = B \exp\left(\frac{\sigma\sqrt{a}}{KT}\right)$$

The above correlations, of course, are limited to experimental geometries where the stress intensity factors are well known, and generally to crack velocities considerably less than the elastic wave speeds in the material under consideration. In many nonmetallic materials, the range of stress intensities (i.e., combinations of crack size and stress) over which moderate velocity crack growth occurs is very narrow.

For such materials, it is convenient to define an approximate critical stress intensity above which unstable crack growth occurs at a high velocity and below which essentially no growth will occur. In an analogous manner, some materials exhibit a small range of breaking strengths, and for such materials it is convenient to define a single material strength.

In the present work, the intent is specifically not to make either of these two assumptions. The consequence is to introduce a certain amount of additional mathematical labor, but allow the description of additional aspects of the impact process. The benefits and shortcomings of this approach is discussed.

4.3 Method of Micromechanics Analysis

4.3.1 Stress Analysis of Impact

As discussed previously, the Hertz model provides a good description of the peak stress distribution associated with solid spherical impact. This approximation

is a good model if the ratio of the contact radius to contact time is small relative to the shear and longitudinal wave velocities. Low velocity impact will, therefore, be assumed to be well described by the Hertz model for the purposes of this study.

4.3.2 Crack Propagation

The crack growth will be approximated by the empirical crack velocity versus crack tip stress intensity relationships. For convenience, the polynomial form is used. This specific relationship has the disadvantage that under constant stress conditions for a finite time, infinite crack growth rates and sizes can be predicted. To circumvent this mathematical characteristic, the crack propagation velocity is taken as the shear wave speed if the empirical relationship predicts crack velocities in excess of the shear wave speed.

This modification is, admittedly, somewhat arbitrary, but is consistent with the concept of cracks rapidly accelerating to a speed approximating the shear wave speed. An alternative approach of fitting the empirical data to a mathematical relationship which contained an upper limiting crack velocity would produce qualitatively similar results. With the current state of knowledge on the theory of crack growth, arbitrariness must be introduced in any attempt to extrapolate observed low velocity to high velocities. However, because of the rapid transition to sonic velocities of propagation, such details may assume lesser importance than implied by first consideration.

4.3.3 Crack Initiation

Three approaches may be taken for this aspect of the problem. The first is to assume the material is free of microstructural features such as microcracks, and that microcracks are nucleated by mechanisms such as crystallographic slip in grains, stress concentrations around pores, inclusions, or agglomeration of such microstructural features. The second is to assume that the effect of such nucleation processes is an initial crack size. The third is to assume that the cracks are pre-existing, albeit very small. For many purposes, the second and third approaches

are equivalent. The nucleation approach has appeal for formulating materials of complex microstructure, but the prediction of size of the nucleated crack is not straightforward.

The approach taken is that the cracks are treated as pre-existing, and that the size distribution is related to the failure strength distribution observed in slow loading environments; e.g., tensile testing and/or static indentation. The specific details are considered to be obtained from the integration of the crack growth relationships. The condition of fracture for a uniformly stressed material is that the crack should grow to a size comparable with the dimensions of the specimen. For the power law of crack velocity, it is convenient to define fracture as equivalent to predicted crack growth to infinite size. Under constant loading rate conditions, the fracture condition may be written as

$$\left\{\frac{2(n+1)}{A(n-2)}\,\dot{\sigma}\right\}^{\frac{1}{n+1}} = \sigma\, a_o^{\frac{n-2}{2(n+1)}}$$

or

$$= \sigma\, a_o^{\frac{1}{2}\left(1-\frac{3}{n+1}\right)}$$

For large values of the exponent in the crack velocity equations (i.e., sharp transition between slow and rapid growth), the strength is approximately proportional to the inverse square root of initial crack size, and is not highly dependent upon the loading rate. The Griffith criterion is well satisfied under these conditions. As the exponent n decreases, the transition from slow to rapid growth occurs over a wider range of test conditions, the dependence of strength on load rate becomes more significant, and the Griffith criterion becomes a poorer approximation. Qualitatively, similar considerations will result from other crack velocity relationships. The essential point of the discussion is that if the dynamics of crack growth are known, then the strength and strength distributions of the material can be used to infer characteristics of the flaw size distribution.

4.4 Micromechanics Analyses

4.4.1 Solid Versus Liquid Particle Impact

The stress analyses have confirmed the Rochester and Brunton experiments (Refs. 1, 2) which indicated that off-axis pressure peaks occur as a result of liquid (not solid) particle impact. The phenomenon is apparently real and there is a simple explantion (Section 2.0). Therefore, the mechanics of liquid and solid impact are quantitatively different which is an extremely important conclusion for guiding material test development. This can be built upon through micromechanical considerations to relate the observed differences in material response.

The mechanics were aptly summarized in Figure 9, wherein the rate of increase of contact radius, speed of sound in water, and peak surface contact pressure are given as a function of time. The peak off-axis pressure occurs when the speed of sound and the velocity of surface contact are approximately identical. Under these conditions, the physical events occurring at the outer contact point are sensitive to the pressures developed earlier (more central to the contact area) and a pressure superposition occurs which gives rise to the exceedance of the water hammer pressure.

The relationship to materials response is as follows. Building on the concept that in liquid impact, the surface pressure drives the propagation of surface crack nuclei, Figure 30, the concept that crack growth obeys laws similar to those found for crack growth studies, Figure 31, the idea that the driving force for solid impact crack growth is the surface Hertizian stress, Figure 32, then the solid and liquid impact damage initiation (onset of mass loss) by Adler, Figure 33, can be reconciled. This reconciliation is given in Figure 34.

Figure 34 shows the improved theoretical correlation with the solid and liquid impact experiments which resulted from the analyses.

While this is not a correlation for all of the observations on similarities and differences between solid and liquid impact, more detailed coupling of the

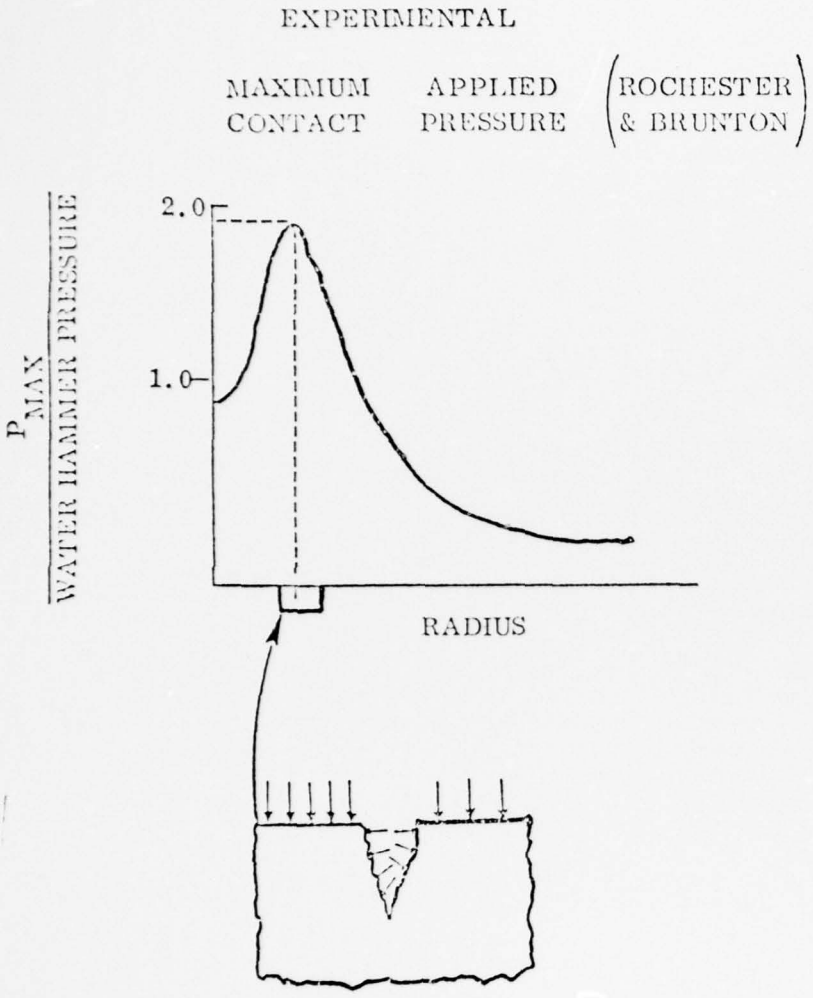

- THE EXPERIMENTAL PRESSURE 1.8 * WATER HAMMER PRESSURE
- WATER CAN ENTER SURFACE CRACKS
- *THE EFFECTIVE TENSILE CRACK* OPENING STRESS APPROXIMATES THE MAXIMUM PRESSURE
- THIS CONDITION DOES NOT OPERATE FOR SOLID IMPACTS

Figure 30. Water Drop Impact and Cracks

- IF $\frac{da}{dt} = \lambda(\sigma\sqrt{\pi a})^n$ and $a(t=0) = a_o$
- THEN CRACKS GROW TO SUBSTANTIAL SIZE WHEN

$$\Delta t \sigma^n = \frac{(n-2)}{2\lambda} \cdot a_o^{-\left(\frac{n-2}{2}\right)}$$

- FOR MULTIPLE IMPACTS, N, $\Delta t \simeq N$

$$\therefore N\sigma^n = \varphi^*$$

CRACK GROWTH DATA (25°C)

$n \simeq 20$

$\lambda_{WATER}^{-1} \simeq .01 - .10\, \lambda_{AIR}$

(REF. WIEDERHORN)

IMPACT DATA FOR MEASURABLE DATA

PARTICLE	VELOCITY (M/SEC)	CALCULATED TENSILE STRESS	N
GLASS	61	1.15×10^9	18×10^3
GLASS	114	1.55×10^9	$.3 \times 10^3$
WATER	222	$\simeq 7.0 \times 10^8$	$.5 \times 10^3$

(REF. ADLER)

Figure 31. Tentative Application, Crack Growth Laws

- HERTZ ANALYSIS FOR STRESS ESTIMATION
- OH AND FINNIE STATIC FLEXURAL FRACTURE STATISTICS AND PDA PROBABILITY CRITERIA ON 7740 PYREX TO RELATE STRESSES TO CRACKING OR CRACK SOURCE ACTIVATION PROBABILITIES

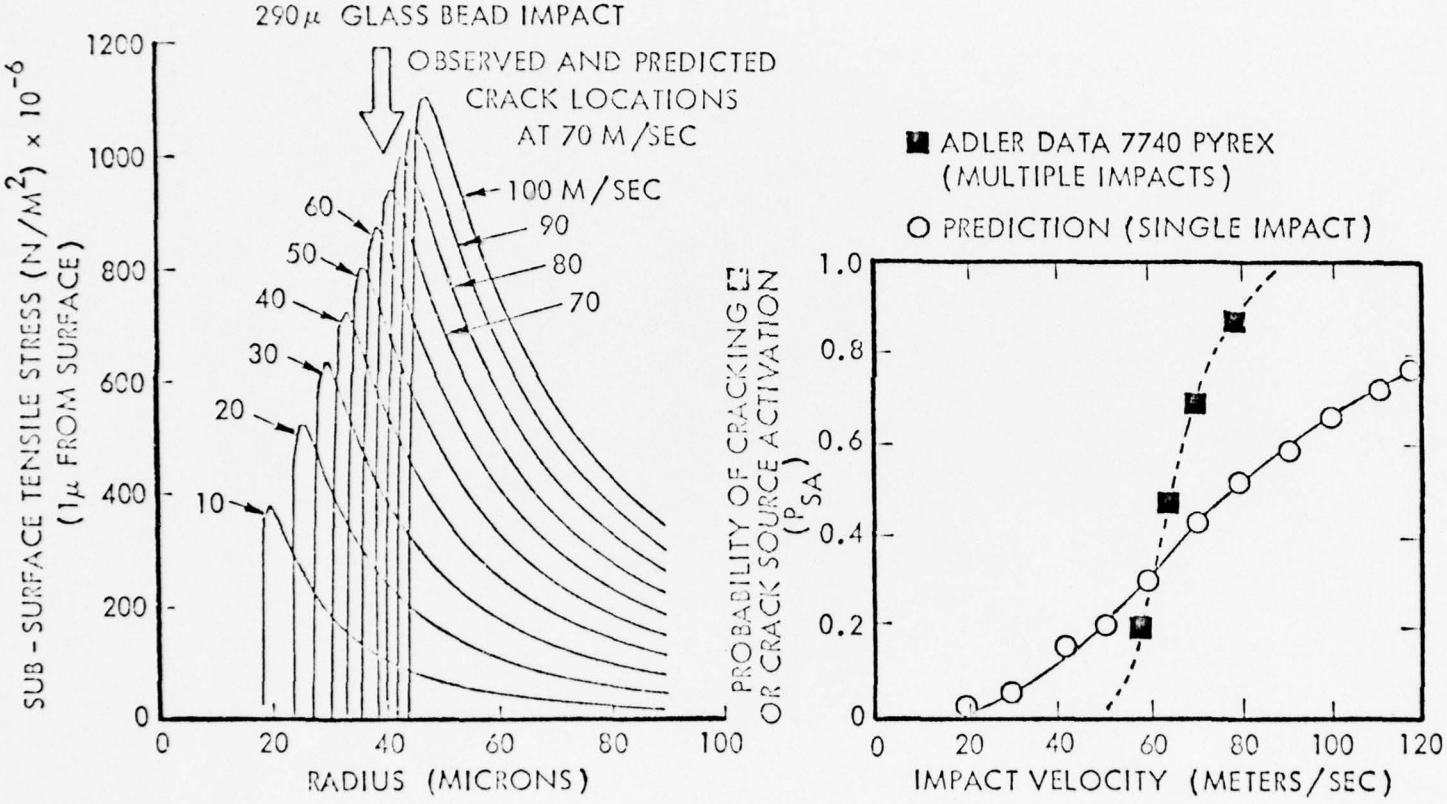

- REASONABLE FIRST ORDER STATIC-IMPACT CORRELATION
  - ▲ POSSIBLE IMPROVEMENT USING CRACK GROWTH MODELS (NOT ALL ACTIVATED CRACK SOURCES WILL GROW VISIBLE CRACKS DURING THE IMPACT TIME)
  - ▲ INCORPORATE EXPLICIT MULTIPLE IMPACT/TIME HISTORY CONSIDERATIONS

Figure 32. Tentative Application to Solid Impact

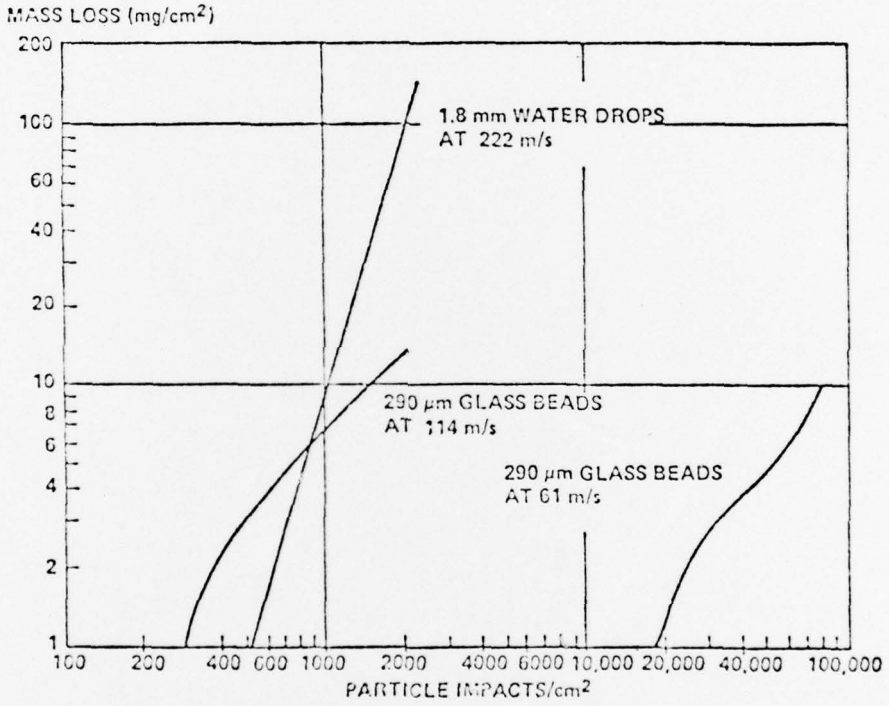

Figure 33. Erosion Rates for Borosilicate Glass Due to Multiple Collisions by 1.8 mm Water Drops and 290 μm Glass Beads

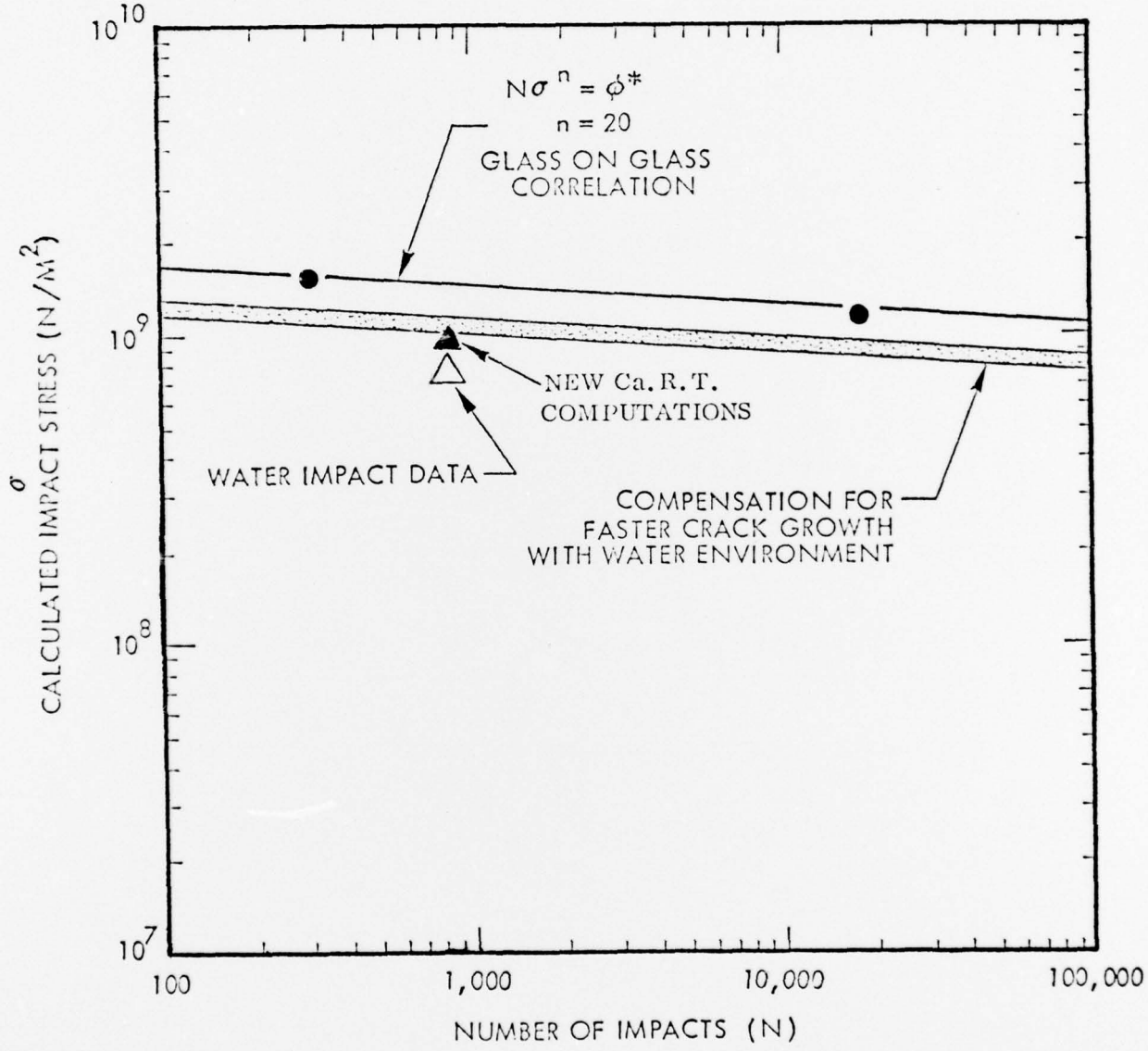

Figure 34. Calculated Impact Stress Versus Number of Impacts

mechanics and micromechanics will provide the required understanding. Much of this methodology can result from further interrogation of the present computations.

4.4.2 Surface Finish

L. A. Glenn (Ref. 8) experimentally examined the impact of steel cylinders on SIAl and 20 percent Pb0 glass blocks with and without surface etching to modify brittle fracture strength ($\simeq 200\mu$ material removal). Impacting conditions were 14 mm diameter x 14 mm long cylinders at 100 and 300 meters/second. The fracture patterns for etched versus unetched were quite different in shape and size. Asymmetric fracture was common, but is probably related to the experimental difficulty of getting good impact alignment with cylindrical projectiles. There is a strong possibility that it has some association with the flaw statistics. The etched fractures are related to fracture initiation in depth and the unetched fractures are related to surface nucleated fracture.

There are many implications stemming from the present comparison. It is well known by the producers of IR domes that surface finish is one of the more important aspects of production and by some small companies is quite proprietary. The good surface finish can cost more than basic dome fabrication. Another application is that as impact velocity is increased beyond Mach 1, the dynamical (wave propagation) phenomena will become more and more evident, and the deficiencies of the Hertz model or any static model as a basis for data correlation will become more prominent.

5.0 CONCLUSIONS

The following conclusions have been reached as a result of the Erosion Mechanics and Micromechanics Program:

- Dynamic stress analyses performed under this contract have demonstrated correlation with Rochester and Brunton's experiments which indicated that off-axis pressure peaks occur during liquid particle impact. Therefore, the mechanics of impact are significantly different for liquid versus solid particles and can be expected to influence material response.

- At low velocity, solid particle impact varies from liquid particle impact in the following ways:

  - Solid particles produce higher and more localized peak surface pressures on-axis.
  - Solid particles produce higher magnitudes of pressure acting over shorter time periods.
  - Solid particles produce higher tensile stresses acting over shorter times.

- Material performance ranking must account for the coupling of mechanics with material response at both macroscopic and microscopic levels and requires a coordinated effort which can treat the various aspects in a logical self-consistent fashion.

- Surface cracks effect the material response during water drop impact. Therefore, surface finish is an important consideration.

- Techniques are available for merging macromechanics (impact stress and strain computations) to micromechanics (materials response, crack initiation, crack propagation) to provide improved material development guidelines.

- The crack propagation considerations provide the fundamental relationship between fatigue behavior and long term erosion behavior.

- Surface finish can provide enhanced fatigue resistance.

- The best approach for crack initiation modeling is to treat the cracks as pre-existing and to infer their size and orientation distributions (statistical) from the failure strength distributions measured in slow loading environments.

- In water impact, the peak off-axis pressure occurs when the speed of sound in the water equals the velocity of surface contact radius.

6.0 REFERENCES

1. Rochester, M. C. and J. H. Brunton, "Influence of Physical Properties of the Liquid on the Erosion of Solids," in Erosion, Wear, and Interfaces with Corrosion, ASTM STP 657, American Society for Testing and Materials, 1974, pp. 128-147.

2. Rochester, M. C. and J. H. Brunton, "Surface Pressure Distribution During Drop Impingement," Report No. CUED/C-MAT/TR 15, Engineering Department, University of Cambridge, Cambridge, England, 1974.

3. Heyman, F. J., J. Appl. Physics, Vol. 40, 1969, pp. 5113-5122.

4. WAVE-L Code, California Research and Technology, Inc., Woodland Hills, California 91364.

5. "A Thiruvengaden," in Erosion by Cavitation or Impingement, STP 408, American Society for Testing and Materials, Philadelphia, 1967, p. 22.

6. Thomas, G. P., "Rain Erosion and Allied Phenomena," Proc. Second Meersburg Conf., Vol. 2, Royal Aircraft Establishment, Fainborough, England, 1968, p. 785.

7. Jolliffe, K. H., Phil. Trans. Roy. Soc., London, Ser. A 260, 1966, p. 101.

8. Glenn, L. A., J. Mech. Phys. Solids, Vol. 24, 1976, pp. 93-106.